Title

The robustness of phase-locking in neurons with dendro-dendritic electrical coupling

Journal

Journal of Mathematical Biology, 68(1-2)

ISSN

0303-6812

Authors

Schwemmer, Michael A
Lewis, Timothy J

Publication Date

2014

DOI

10.1007/s00285-012-0635-5

Peer reviewed

J. Math. Biol. (2014) 68:303–340
DOI 10.1007/s00285-012-0635-5

Mathematical Biology

The robustness of phase-locking in neurons with dendro-dendritic electrical coupling

Michael A. Schwemmer · Timothy J. Lewis

Received: 7 May 2012 / Revised: 13 September 2012 / Published online: 22 December 2012

Abstract We examine the effects of dendritic filtering on the existence, stability, and robustness of phase-locked states to heterogeneity and noise in a pair of electrically coupled ball-and-stick neurons with passive dendrites. We use the theory of weakly coupled oscillators and analytically derived filtering properties of the dendritic coupling to systematically explore how the electrotonic length and diameter of dendrites can alter phase-locking. In the case of a fixed value of the coupling conductance (g_c) taken from the literature, we find that repeated exchanges in stability between the synchronous and anti-phase states can occur as the electrical coupling becomes more distally located on the dendrites. However, the robustness of the phase-locked states in this case decreases rapidly towards zero as the distance between the electrical coupling and the somata increases. Published estimates of g_c are calculated from the experimentally measured coupling coefficient (CC) based on a single-compartment description of a neuron, and therefore may be severe underestimates of g_c. With this in mind, we re-examine the stability and robustness of phase-locking using a fixed value of CC, which imposes a limit on the maximum distance the electrical coupling can be

M. A. Schwemmer
Program in Applied and Computational Mathematics and Princeton Neuroscience Institute, Princeton University, Princeton, NJ 08544, USA

T. J. Lewis
Department of Mathematics, University of California, Davis, One Shields Ave., Davis, CA 95616, USA

Present address:
M. A. Schwemmer (✉)
Mathematical Biosciences Institute, The Ohio State University, Jennings Hall 3rd Floor, 1735 Neil Ave., Columbus, OH 43210, USA
e-mail: schwemmer.2@mbi.osu.edu

located away from the somata. In this case, although the phase-locked states remain robust over the entire range of possible coupling locations, no exchanges in stability with changing coupling position are observed except for a single exchange that occurs in the case of a high somatic firing frequency and a large dendritic radius. Thus, our analysis suggests that multiple exchanges in stability with changing coupling location are unlikely to be observed in real neural systems.

Keywords Mathematical Neuroscience · Ball-and-stick neuronal model · Phase response curves · Electrical Coupling · Dendrites · Synchronization

Mathematics Subject Classification (2000) 92B25 · 37N25

1 Introduction

Synchronization of oscillatory electrical activity in neuronal networks has been observed in many neural systems and has been linked to various behavioral functions such as feeding, breathing, and locomotion (Ono et al. 1986; Rekling and Feldman 1998; Tresch and Kiehn 2002). In the mammalian cortex, these oscillations have been hypothesized to be involved in cognition and sensory information processing, (e.g., Averbeck and Lee 2004; Ward 2003), however their precise functional role is the topic of much debate. Nonetheless, recent experimental and theoretical studies have shed light on the mechanisms underlying cortical oscillations (Cardin et al. 2009; Gonzalez-Burgos and Lewis 2008; Kopell and Ermentrout 2003; Lewis and Rinzel 2003; Mancilla et al. 2007; Mann and Paulsen 2005; Salinas and Sejnowski 2011). Results from many of these studies suggest that networks of inhibitory neurons play a fundamental role in generating the oscillatory electrical behavior seen in the mammalian neocortex (Buzsáki and Draguhn 2004; Buzsáki 1997; Cardin et al. 2009; Gonzalez-Burgos and Lewis 2008; McBain and Fisahn 2001; Sohal et al. 2009; Wang and Buzsáki 1996). Direct electrical recordings have revealed that inhibitory neurons are highly interconnected by electrical synapses (Amitai et al. 2004; Connors and Long 2004; Galaretta and Hestrin 1999; Gibson et al. 1999), and evidence suggests that this electrical coupling helps to coordinate synchronous oscillatory behavior (Beierleinet al. 2000; Gibson et al. 2005; Hestrin and Galarreta 2005; Mancilla et al. 2007; Saraga et al. 2006; Traub et al. 2001).

Most theoretical studies that examine the synchronization properties of inhibitory networks model neurons as single-compartment objects, ignoring the spatial anatomy of the cell. This simplification is made for mathematical tractability and computational efficiency. However, many neurons are not electrotonically compact, and single-compartment models cannot be expected to fully capture their behavior. Indeed, previous work has shown that dendritic properties can have significant effects on neuronal firing dynamics at the single cell level (Mainen and Sejnowski 1996; Schwemmer and Lewis 2011, 2012), and in network synchronization (Bressloff and Coombes 1997; Crook et al. 1998; Lewis and Rinzel 2004; Remme et al. 2009; Saraga and Skinner 2004; Saraga et al. 2006; Zahid and Skinner 2009). This is true even if the dendrites are passive. Experimental studies have revealed that cortical inhibitory neu-

rons are highly interconnected by electrical synapses on their dendrites (Amitai et al. 2004; Fukuda and Kosaka 2000, 2003; Fukuda et al. 2006). Furthermore, the dendrites of these inhibitory neurons appear to display effectively passive electrical behavior (Hu et al. 2010). This suggests that passive dendritic properties and electrical coupling may play an important role in the synchronization of inhibitory networks, and, consequently, in the generation of the observed synchronous electrical activity in the cortex. Therefore, it is necessary to understand how dendritic filtering affects synchronization patterns and their robustness.

The effects of dendritic properties on the phase-locking behavior of neurons coupled with dendro-dendritic electrical synapses have been examined in previous studies. Lewis and Rinzel (2004), Saraga and Skinner (2004), Saraga et al. (2006), and Zahid and Skinner (2009) explored these effects using multi-compartmental neuronal models. These studies find that dendritic properties can significantly influence phase-locking behavior in neuronal networks, but they did not examine the detailed mechanisms by which dendritic filtering affects phase-locking. Crook et al. (1998) and Bressloff and Coombes (1997) directly examined the mechanism by which dendritic filtering affects the existence and stability of phase-locking in spatially extended neurons coupled with dendro-dendritic *chemical* synapses. However, these studies on chemical synapses, as well as the aforementioned studies on electrical synapses, lacked a systematic exploration of the robustness of phase-locking to heterogeneity and noise. There are varying levels of heterogeneity and noise in real neuronal networks, and therefore, when interpreting the results of modeling studies, one must also consider the robustness of the phase-locked states to get a complete picture. If a phase-locked state in a neuronal network model is not robust, then it is highly unlikely that it will be observed in a real neural system.

Using a formalism similar to Crook et al. (1998) and Bressloff and Coombes (1997), we examine the effects of dendritic filtering on the existence and stability of phase-locked states in a pair of electrically coupled neurons, and we include a systematic exploration of the robustness of phase-locked states to heterogeneity and noise. Each neuron is modeled as an isopotential somatic oscillator attached to a passive dendritic cable using the "ball-and-stick" model (Rall 1960). The two ball-and-stick neurons are coupled via an electrial synapse located at the distal end of their dendrites. We use the theory of weakly coupled oscillators (Ermentrout and Kopell 1984; Kuramoto 1984; Neu 1979; Schwemmer and Lewis 2012) to derive a single scalar differential equation that governs the dynamics of the phase-difference between the two ball-and-stick neurons. This equation inlcudes an analytical representation of the filtering properties of the dendritic coupling. We then use the phase model to systematically explore how the electrotonic length, dendritic diameter and electrical coupling strength can alter the stability and robustness of phase-locked states to heterogeneity in intrinsic firing frequency. We extend our phase model to incorporate heterogeneities in dendritic parameters, e.g., heterogeneity in dendritic length, and explore the stability and robustness of phase-locking in light of these additional heterogeneities. Lastly, we show that qualitatively similar results hold when considering robustness of phase-locking to noise.

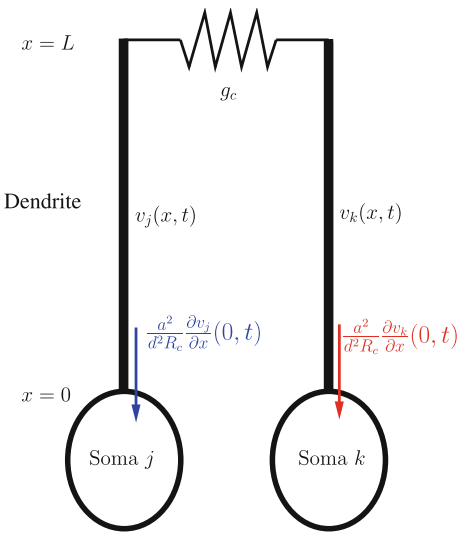

Fig. 1 Two electrically coupled ball-and-stick neurons. Each neuron is modeled as a ball-and-stick neuron, which consists of an active soma attached to a thin passive dendritic cable. The two neurons are then electrically coupled by a linear ohmic resistor with conductance g_c at the distal ($x = L$) end of the dendrite. The terms next to the *arrows* represent axial currents flowing between the dendrites and the somata

2 Electrically coupled ball-and-stick model

We consider a model of a pair of spatially extended neurons that are coupled by an electrical synapse located between the dendrites of the neurons. We model the electrical activity of the isolated neurons using the "ball-and-stick" model (Bressloff and Coombes 1997; Crook et al. 1998) that consists of a spherical active isopotential soma attached to a single thin passive dendrite. We make the assumption that the electrical synapse between the two neurons is located at the distal end of the dendrite (see Fig. 1). This assumption is made for ease of mathematical computation, but could be relaxed to place the synapse at any point along the dendrite (e.g., Bressloff and Coombes 1997). We initially assume that the two neurons are identical, but we introduce heterogeneity in Sect. 3.2.

The dendrite of each neuron is modeled as a one-dimensional passive cable of physical length L (Rall 1957, 1977)

$$C_m \frac{\partial v_j}{\partial t} = \frac{a}{2R_i}\frac{\partial^2 v_j}{\partial x^2} - g_{LD}(v_j - E_{LD}), \quad x \in (0, L), \tag{1}$$

where $v_j(x,t)$ is the voltage (in mV) in the dendrite of the jth neuron at position x and time t (in ms), g_{LD} is the leakage conductance in the dendrite (in mS/cm^2), R_i is the internal resistivity of the dendrite (in kΩ cm), a is the radius of the dendrite (in cm), E_{LD} is the leakage channel reversal potential of the in the dendrite (in mV), and C_m is the specific membrane capacitance (in μF/cm^2).

Hodgkin–Huxley (HH) type equations are used to model the electrical activity of each soma. An application of the conservation of current law at the junction connecting the spherical soma and the dendrite ($x = 0$) yields the equation for the proximal

boundary condition

$$C_m \frac{\partial v_j}{\partial t}(0,t) = -I_{ion,S}(v_j(0), \vec{w}) + I + \frac{a^2}{d^2 R_i} \frac{\partial v_j}{\partial x}(0,t), \tag{2}$$

where $I_{ion,S}(v_j, \vec{w})$ (in μA/cm^2) represents the sum of the HH-type ionic currents in the jth soma, $\vec{w}$ is a vector containing the gating variables of the ionic conductances, and d is the diameter of the soma (in cm). The gating variables in the vector $\vec{w}$ are described by equations of the form

$$\frac{d\vec{w}}{dt} = \frac{1}{\tau_{\vec{w}}}(\vec{w}_\infty(v) - \vec{w}). \tag{3}$$

The last term in Eq. (2) represents the axial current flowing between the dendrite and the soma. The parameter I is the somatic bias current (in μA/cm^2). Note that changes in I are equivalent to changes in the leakage reversal potential of the somata, E_L, and could be thought of as being due to either externally applied current to the soma or the effects of a neuromodulator. The values of I and E_L are chosen such that the isolated soma undergoes asymptotically stable T-periodic (limit cycle) oscillations. We define $v_{LC}(t)$ to be the membrane potential component of each isolated somata's limit cycle.

The two neurons are electrically coupled at the distal end ($x = L$) of their respective dendrites (see Fig. 1). Invoking conservation of current once again yields the distal boundary condition

$$\frac{1}{R_i} \frac{\partial v_j}{\partial x}(L,t) = \frac{g_c}{\pi a^2}(v_k(L,t) - v_j(L,t)), \tag{4}$$

where the electrical synapse is modeled as a linear ohmic resistor with conductance g_c in units of mS. It is important to note that the term $\frac{a^2}{d^2 R_i} \frac{\partial v_j}{\partial x}(0,t)$ in Eq. (2) incorporates the effects of the electrical coupling and the dendrites on the dynamics of the somatic oscillators.

This model is similar to the one studied by Crook et al. (1998) except for the fact that they studied two ball-and-stick neurons coupled with chemical synapses rather than electrical coupling. In all the simulations presented here, we use the fast-spiking (FS) interneuron model of Erisir et al. (1999). However, the basic analysis that we employ is general and can be applied to any oscillatory somatic dynamics with similar results.

The subsequent analysis relies on a certain combination of model parameters being sufficiently "small". To identify this small compound parameter, we nondimensionalize the model (1–4). We set $V_j = V_j(\bar{x}, \bar{t}) = \frac{v_j(\lambda x, \tau_D \bar{t})}{-E_L}$ (where E_L is the leakage reversal potential in the soma), $\bar{x} = \frac{x}{\lambda}$, $\bar{t} = \frac{t}{\tau_D}$, $\lambda = \sqrt{\frac{a}{2R_i g_{LD}}}$ is the length constant of the dendrite, and $\tau_D = \frac{C_m}{g_{LD}}$ is the membrane time constant of the dendrite. The resulting nondimensional equations for the coupled ball-and-stick model neurons are

$$\begin{cases} \frac{\partial V_j}{\partial \bar{t}} = \frac{\partial^2 V_j}{\partial \bar{x}^2} - (V_j - \overline{E}_{LD}) \\ \frac{\partial V_j}{\partial \bar{t}}(0,\bar{t}) = -\overline{I}_{ion,S}(V_j(0,\bar{t}),\vec{w}) + \overline{I} + \varepsilon \frac{\partial V_j}{\partial \bar{x}}(0,\bar{t}) \\ \frac{\partial V_j}{\partial \bar{x}}\left(\frac{L}{\lambda},\bar{t}\right) = g\left(V_k\left(\frac{L}{\lambda},\bar{t}\right) - V_j\left(\frac{L}{\lambda},\bar{t}\right)\right) \end{cases} \tag{5}$$

where $j,k = 1,2$ with $j \neq k$, $\frac{L}{\lambda}$ is the electrotonic length of the dendrite, $\overline{E}_{LD} = \frac{E_{LD}}{-E_L}$, $\overline{I}_{ion,S}(V_j(0,\bar{t}),\vec{w}) = \frac{1}{-g_{LD}E_L} I_{ion,S}((-E_L)V_j(0,\bar{t}),\vec{w})$, $\overline{I} = \frac{1}{-g_{LD}E_L} I$, and

$$g = \frac{g_c R_i \lambda}{\pi a^2} \tag{6}$$

$$\varepsilon = \frac{a^2}{d^2 g_{LD} R_i \lambda}. \tag{7}$$

Also, Eq. (3) becomes $\frac{d\vec{w}}{d\bar{t}} = \frac{\tau_D}{\tau_{\vec{w}}}(\vec{w}_\infty(-E_L V_j(0,\bar{t})) - \vec{w})$. We also define the nondimensionalized period of the limit cycle to be $\overline{T} = \frac{T}{\tau_D}$, and the nondimensional voltage component of the isolated somata's limit cycle as $V_{LC}(\bar{t})$.

The term $\varepsilon \frac{\partial V_j}{\partial \bar{x}}(0,\bar{t})$ in Eq. (5) is the axial current at the soma-dendritic junction and is the perturbation to the jth soma's membrane potential dynamics and incorporates the effects of the electrical coupling. This perturbation will be weak if

$$\varepsilon = \frac{a^2}{d^2 g_{LD} R_i \lambda} = \frac{a^2}{d^2}\sqrt{\frac{2}{g_{LD} R_i a}}$$

is small. One interpretation of ε being small is if $a \ll d$, i.e., if the radius of each dendrite is small relative to the diameter of each of the somata, and if $\sqrt{\frac{2}{g_{LD} R_i a}}$ is $O(1)$ or less so that $\varepsilon \ll 1$.

3 Theory of weak coupling and reduction to a phase model

The theory of weak coupling (Ermentrout and Kopell 1984; Kuramoto 1984; Neu 1979; Schwemmer and Lewis 2012), has been widely used to analyze dynamics in networks of oscillating neurons (e.g., Ermentrout 1996; Hoppensteadt and Izikevich 1997; Lewis and Rinzel 2003; Pfeuty et al. 2003; Schwemmer and Lewis 2012). Consider a network of weakly coupled neurons such that each neuron when isolated from the network displays $\overline{T}$-periodic limit cycle oscillations. In this case, the complete state of each neuron can be approximated by its phase on its $\overline{T}$-periodic limit cycle, $\theta_j(\bar{t}) = \overline{\omega}\bar{t} + \phi_j(\bar{t}) \in [0,1)$, where $\overline{\omega} = \frac{1}{\overline{T}}$ is the non-dimensional frequency of the unperturbed oscillations and $\phi_j(\bar{t})$ is the relative phase of the jth neuron. Thus, this theory enables one to significantly reduce the number of equations that describe a neuronal network: a system that has N neurons each described by M equations can be reduced to a system of N equations that describe the evolution of each neurons' phase variable $\theta_j(t)$. For a pair of coupled neurons, the dynamics of the system can be further

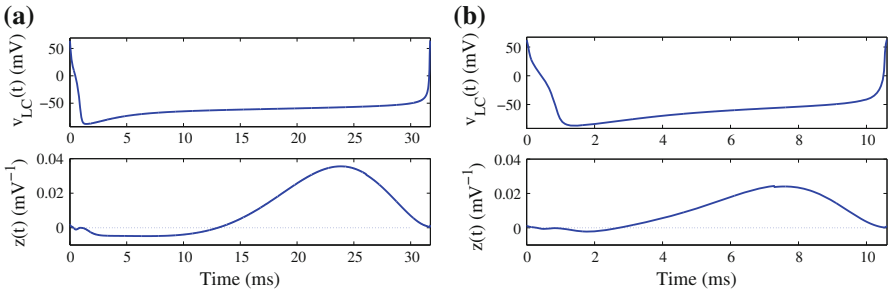

Fig. 2 Voltage component of the limit cycle and phase response curves. The voltage component of the limit cycle (*upper plots*) along with the corresponding phase response curve (*lower plots*) are plotted as a function of time for two different firing frequencies **a** 31 Hz and **b** 94 Hz

reduced to the consideration of a single scalar differential equation that describes the evolution of the phase difference between the two neurons, $\phi = \theta_k - \theta_j = \phi_k - \phi_j$.

According the theory of weakly coupled oscillators, the evolution of the jth neuronal oscillator's relative phase is governed by the phase equation

$$\begin{aligned} \frac{d\phi_j}{d\bar{t}} &= \frac{1}{\overline{T}} \int_0^{\overline{T}} Z(s) I_{coupl}(s; \overline{T}(\phi_k - \phi_j)) ds \\ &= H(\phi_k - \phi_j), \quad j,k = 1,2;\ j \neq k, \end{aligned} \tag{8}$$

where $H(\phi_k - \phi_j)$ is known as the interaction function and describes the modulation of the jth oscillator's instantaneous frequency resulting from the coupling current, $I_{coupl}(s; \overline{T}(\phi_k - \phi_j))$. Note that $I_{coupl}(s; \overline{T}(\phi_k - \phi_j))$, and therefore $H(\phi_k - \phi_j)$, is a function of the difference between the relative phases of neuron j and neuron k, $\phi_k - \phi_j$. $Z(s)$ is the infinitesimal phase response curve (PRC) of the somatic oscillator. The PRC quantifies the change in phase due to a δ-function current perturbation at a particular phase on the limit cycle. The PRC can be computed by perturbing the isolated neuron with a small brief current pulse at various different phases along its cycle and measuring the resulting change in period (Netoff et al. 2012). Alternatively, the PRC for model neurons can be found by computing the solution to the adjoint problem of the system linearized around its limit cycle (Schwemmer and Lewis 2012). For reference, Fig. 2 plots the voltage component of the limit cycle and the corresponding phase response curve of the FS interneuron model of Erisir et al. (1999) for the two different firing frequencies that we utilize in illustrating our results. The integral in the phase model (8) is the average of $Z(s)I_{coupl}(s; \overline{T}(\phi_k - \phi_j))$ over one period of the oscillations and stems from the fact that changes in the relative phase of the neuron ϕ_j occur on a time scale much slower than the period of the unperturbed oscillations $\overline{T}$.

3.1 Phase model for the electrically coupled ball-and-stick neurons

The theory of weak coupling can be applied to the electrically coupled ball-and-stick neurons by considering the "somato-dendritic current" as the weak perturbation to the

somata, following Bressloff and Coombes (1997), Crook et al. (1998), Remme et al. (2009), and Schwemmer and Lewis (2011). Note that, because of the construction of the electrically coupled ball-and-stick neuron and assumption that the dendrite only weakly affects the somatic dynamics, the somata are considered to be the oscillatory units in our system. Therefore, in order to use the theory of weakly coupled oscillators, we only need the PRC for the somatic oscillator. The dendritic dynamics are considered to be part of the coupling structure and, thus, incorporated into the perturbation to the oscillatory somatic dynamics. During oscillations in the coupled ball-and-stick model, a current flows between the electrical synapse connecting the two cells, and between the soma and the dendrite of each of the two neurons. The somato-dendritic current that modulates the intrinsic frequency of the jth somata is given by

$$I_{coupl}(s; \overline{T}(\phi_k - \phi_j)) = \varepsilon \frac{\partial V_j}{\partial \overline{x}}(0, s) \tag{9}$$

in the phase model (8). As written, $\varepsilon \frac{\partial V_j}{\partial \overline{x}}(0, s)$ does not have an explicit dependence on the phases of the two neurons. To obtain the explicit dependence of the somato-dendritic current on phase, we compute the solution of the coupled ball-and-stick system (5) to leading order in ε (i.e., we set $\varepsilon = 0$). In this case, the somatic ($\overline{x} = 0$) boundary condition corresponds to the isolated somatic dynamics: $V_j(0, \overline{t}) = V_{LC}(\overline{t} + \overline{T}\phi_j)$, where $V_{LC}(\cdot)$ is the voltage component of isolated somata's limit cycle. The dependence on ϕ_j in $V_j(0, \overline{t}) = V_{LC}(\overline{t} + \overline{T}\phi_j)$ stems from the assumption that the perturbations to the oscillator are weak enough to only affect how quickly the oscillator moves around its limit cycle. This approximation simplifies the boundary condition at the soma ($\overline{x} = 0$) and yields the leading order approximation for the dendritic dynamics

$$\begin{cases} \frac{\partial V_j}{\partial \overline{t}} = \frac{\partial^2 V_j}{\partial \overline{x}^2} - (V_j - \overline{E}_{LD}) \\ V_j(0, \overline{t}) = V_{LC}(\overline{t} + \overline{T}\phi_j) \\ \frac{\partial V_j}{\partial \overline{x}}\left(\frac{L}{\lambda}, \overline{t}\right) = g\left(V_k\left(\frac{L}{\lambda}, \overline{t}\right) - V_j\left(\frac{L}{\lambda}, \overline{t}\right)\right). \end{cases} \tag{10}$$

System (10) is a set of two coupled first-order linear partial differential equations with $\overline{T}$-periodic forcing at one end, and a robin boundary condition at the distal end where the electrical coupling is situated. Therefore, the dendritic membrane potential $V_j(\overline{x}, \overline{t})$ can be obtained in the form of a Fourier series. Expanding the somatic potential in a Fourier series,

$$V_{LC}(\overline{t} + \overline{T}\phi_j) = \frac{1}{\overline{T}} \sum_{n \in \mathbb{Z}} V_n e^{2\pi i n(\overline{t} + \overline{T}\phi_j)/\overline{T}}, \tag{11}$$

and solving system (10) yields

$$V_j(\overline{x},\overline{t};\overline{T}\phi_j,\overline{T}\phi_k) = \left[\left(\frac{V_0}{\overline{T}}-\overline{E}_{LD}\right)(c_0+d_0)\right]\sinh(\overline{x})+\left(\frac{V_0}{\overline{T}}-\overline{E}_{LD}\right)\cosh(\overline{x}) + \frac{1}{\overline{T}}\sum_{n\neq 0}\left[V_n\left(\frac{1}{b_n}c_n e^{2\pi i n\overline{T}\phi_k/\overline{T}}+\frac{1}{b_n}d_n e^{2\pi i n\overline{T}\phi_j/\overline{T}}\right)\sinh(b_n\overline{x}) + V_n e^{2\pi i n\overline{T}\phi_j/\overline{T}}\cosh(b_n\overline{x})\right]e^{2\pi i n\overline{t}/\overline{T}}+\overline{E}_{LD} \tag{12}$$

where $b_n = \sqrt{1+2\pi i n/\overline{T}}$ and

$$c_n = \frac{g}{\cosh^2\left(b_n\frac{L}{\lambda}\right)+\frac{g}{b_n}\sinh\left(2b_n\frac{L}{\lambda}\right)} \tag{13}$$

$$d_n = \frac{g^2}{b_n}\frac{1}{\cosh^2\left(b_n\frac{L}{\lambda}\right)}\frac{1}{2\,(g/b_n)^2\tanh\left(b_n\frac{L}{\lambda}\right)+3(g/b_n)+\coth\left(b_n\frac{L}{\lambda}\right)} - b_n\frac{\sinh\left(b_n\frac{L}{\lambda}\right)+\frac{g}{b_n}\cosh\left(b_n\frac{L}{\lambda}\right)}{\cosh\left(b_n\frac{L}{\lambda}\right)+\frac{g}{b_n}\sinh\left(b_n\frac{L}{\lambda}\right)}. \tag{14}$$

Differentiating $V_j(\overline{x},\overline{t};\overline{T}\phi_j,\overline{T}\phi_k)$ (12) with respect to $\overline{x}$, evaluating at $\overline{x}=0$, and multiplying by ε yields the phase-dependent somato-dendritic current into cell j as a function of $\overline{t}$ and parameterized by the phases of the two neurons

$$\tilde{I}_{coupl}(\overline{t};\overline{T}\phi_j,\overline{T}\phi_k)) = \varepsilon\frac{\partial V_j}{\partial\overline{x}}(0,\overline{t};\overline{T}\phi_j,\overline{T}\phi_k) = \varepsilon c_0\left(\frac{V_0}{\overline{T}}-\overline{E}_{LD}\right)+\frac{1}{\overline{T}}\sum_{n\neq 0}\varepsilon c_n V_n e^{2\pi i n(\overline{t}+\overline{T}\phi_k)/\overline{T}} + \varepsilon d_0\left(\frac{V_0}{\overline{T}}-\overline{E}_{LD}\right)+\frac{1}{\overline{T}}\sum_{n\neq 0}\varepsilon d_n V_n e^{2\pi i n(\overline{t}+\overline{T}\phi_j)/\overline{T}} \tag{15}$$

As with standard filtering theory (and cable theory; Koch 1999), c_n and d_n are complex numbers and contain the filtering effects of the dendritic coupling. Specifically, c_n contains the attenuation and phase-shift effects that act on the nth Fourier mode of the membrane potential of soma k. The interpretation of d_n are similar to that of c_n, however, d_n contains the "self-effects" of the jth soma on its own somato-dendritic current.

By substituting the somato-dendritic current as a function of the phase-difference between the two neurons

$$I_{coupl}(\overline{t};\overline{T}(\phi_k-\phi_j)) = \tilde{I}_{coupl}(\overline{t};0,\overline{T}(\phi_k-\phi_j)), \tag{16}$$

into the phase model (8) and expanding the PRC in a Fourier series

$$Z(\bar{t}) = \frac{1}{\overline{T}} \sum_{m \in \mathbb{Z}} Z_m e^{2\pi i m \bar{t}/\overline{T}},$$

we obtain the phase model for the system of coupled ball-and-stick neurons

$$\begin{aligned}
\frac{d\phi_j}{d\bar{t}} &= \frac{1}{\overline{T}} \int_0^{\overline{T}} Z(s)\varepsilon \frac{\partial V_j}{\partial \overline{x}}(0, s, 0; \overline{T}(\phi_k - \phi_j))ds \\
&= \varepsilon c_0 \langle Z \rangle \left(\langle V_{LC} \rangle - \overline{E}_{LD} \right) + \frac{1}{\overline{T}^2} \sum_{n \neq 0} \left[\varepsilon c_n Z_{-n} V_n e^{2\pi i n(\phi_k - \phi_j)} \right] \\
&\quad + \varepsilon d_0 \langle Z \rangle \left(\langle V_{LC} \rangle - \overline{E}_{LD} \right) + \frac{1}{\overline{T}^2} \sum_{n \neq 0} \left[\varepsilon d_n Z_{-n} V_n \right]
\end{aligned} \tag{17}$$

where $\langle V_{LC} \rangle = V_0/\overline{T}$ and $\langle Z \rangle = Z_0/\overline{T}$ are the mean values of $V_{LC}(t)$ and $Z(t)$, respectively.

For convenience of physiological interpretation, the values of all quantities are reported in dimensional terms in the results section. The phase model for the coupled ball-and-stick neurons in dimensional terms is

$$\begin{aligned}
\frac{d\phi_j}{dt} &= \frac{1}{\tau_D} \Bigg(\varepsilon c_0 \langle z \rangle \left(\langle v_{LC} \rangle - E_{LD} \right) + \frac{1}{T^2} \sum_{n \neq 0} \left[\varepsilon c_n z_{-n} v_n e^{2\pi i n(\phi_k - \phi_j)} \right] \\
&\quad + \varepsilon d_0 \langle z \rangle \left(\langle v_{LC} \rangle - E_{LD} \right) + \frac{1}{T^2} \sum_{n \neq 0} \left[\varepsilon d_n z_{-n} v_n \right] \Bigg) \\
&= \frac{1}{\tau_D} H(\phi_k - \phi_j), \quad j, k = 1, 2;\ j \neq k,
\end{aligned}$$

where z_n and v_n are the Fourier coefficients of the dimensional phase response curve and voltage component of the somatic limit cycle, respectively. Note that $z(t)$ has units of mV^{-1}.

Finally, if we set $\phi = \phi_k - \phi_j$ and subtract the respective differential equations for ϕ_k and ϕ_j, we obtain a single differential equation for the evolution of the phase difference of the two identical oscillating coupled ball-and-stick neurons

$$\frac{d\phi}{dt} = \frac{1}{\tau_D} G(\phi), \tag{18}$$

where

$$G(\phi) = \frac{1}{T^2} \sum_{n \neq 0} \varepsilon c_n z_{-n} v_n [e^{-2\pi i n \phi} - e^{2\pi i n \phi}]. \tag{19}$$

Note that the self-effects captured by the d_n terms cancel out in the definition of $G(\phi)$ (when the dendrites are homogeneous).

By analyzing this phase model, we can understand how dendritic properties and electrical coupling affect the phase-locking dynamics of the two ball-and-stick neurons. The zeros of the function $G(\phi)$, ϕ^*, correspond to phase-locked states, i.e., steady-state phase differences between the two neurons. A phase-locked state will be stable if $G'(\phi^*) < 0$, and unstable if $G'(\phi^*) > 0$. Figure 3 shows an example $G(\phi)$ in which both synchrony $\phi_S^* = 0, 1$ and anti-phase $\phi_{AP}^* = 0.5$ are phase-locked states. Only the synchronous state is stable as $G'(\phi_S^*) < 0$, and anti-phase is unstable since $G'(\phi_{AP}^*) > 0$. Thus, for this example, any initial phase difference (other than exactly $\phi(0) = 0.5$) will lead to the two oscillators eventually synchronizing their firing.

3.2 Including heterogeneity in the phase model

The above derivation of the phase model assumed that the two coupled neurons were identical. Neurons are heterogeneous objects. If the heterogeneity is taken to be between the two somata, then the effect of this heterogeneity on the phase model is manifested as a difference in intrinsic firing frequency between the two somata (Kuramoto 1984; Schwemmer and Lewis 2012)

$$\frac{d\phi_j}{dt} = \frac{1}{\tau_D} H(\phi_k - \phi_j) - \frac{\Delta\omega}{2} \tag{20}$$

$$\frac{d\phi_k}{dt} = \frac{1}{\tau_D} H(\phi_j - \phi_k) + \frac{\Delta\omega}{2} \tag{21}$$

where $\Delta\omega$ represents the difference in intrinsic firing frequency between the two neurons. This changes the equation for the phase difference (18) to

$$\frac{d\phi}{dt} = \Delta\omega + \frac{1}{\tau_D} G(\phi). \tag{22}$$

Note that when the dendrites of the two neurons are heterogeneous, $\Delta\omega$ depends on d_n and is no longer constant as in the above equation (see Sect. 6). The phase-locked states are no longer given by the zeros of $G(\phi)$, but rather are given by the intersections of $G(\phi)/\tau_D$ with the line $-\Delta\omega$. The example in Fig. 3 shows that the presence of such a frequency difference $\Delta\omega$ causes the phase-locked states to shift away from pure synchrony and pure anti-phase. As $\Delta\omega$ is increased, the stable and unstable steady-states approach each other and eventually collide in a saddle node bifurcation when the frequency difference is $\Delta\omega^* = \max_\phi \left| \frac{1}{\tau_D} G(\phi) \right|$. For frequency differences greater than $\Delta\omega^*$, no 1:1 phase-locked states exist. That is, $\Delta\omega^*$ represents the maximum amount of frequency heterogeneity between the two oscillators that the system can tolerate before 1:1 phase-locking is lost.

In what follows, we will define the robustness of phase-locking to be the maximum percent frequency heterogeneity possible before 1:1 phase-locking is lost, i.e., $\frac{\Delta\omega^*}{\omega}$ where $\omega = \frac{1}{T}$ is the intrinsic firing frequency of the two somata. Thus, we consider phase-locking in systems with larger $\frac{\Delta\omega^*}{\omega}$ to be more resilient to heterogeneity.

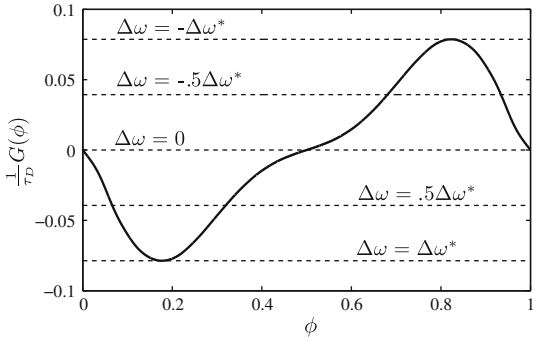

Fig. 3 Phase-locking in the presence of heterogeneity. The figure plots the right hand side of Eq. (18) with an example G function for the case of electrical coupling between the somata ($\frac{L}{\lambda} = 0$) and somatic firing frequency of 31 Hz. The *horizontal dashed lines* represent varying levels of frequency heterogeneity between the two oscillators. Steady-state phase-locked states are represented by the intersections of $\Delta\omega$ and $\frac{1}{\tau_D}G(\phi)$. $\Delta\omega^* = \max_\phi \left|\frac{1}{\tau_D}G(\phi)\right|$ is the largest amount of frequency heterogeneity the system can tolerate before 1:1 phase-locking is completely lost

4 Robustness of phase-locking to heterogeneity in intrinsic frequency

We examine the effects of dendritic properties and electrical coupling on the stability and robustness of phase-locking in the coupled ball-and-stick model. Note that other studies have explored how different intrinsic currents in the soma affect the PRC and thus affect phase-locking (Ermentrout et al. 2001; Fink et al. 2011; Mancilla et al. 2007; Pfeuty et al. 2003). Here, we assume certain particular somatic dynamics and focus on how all of the dendritic parameters affect phase-locking through their influence on the filtering coefficients. However, we stress that our basic results do not fundamentally depend on the specifics of the somatic dynamics. In all figures, we use a model for neocortical FS interneurons due to Erisir et al. (1999) to model the somatic firing dynamics. The values for the parameters of this model as well as dendritic parameters that are held constant are detailed in the Appendix A. We vary the dendritic radius a and the electrotonic length of each dendrite $\frac{L}{\lambda}$ which sets the position of the electrical coupling. We also hold the gap junction conductance g_c constant at a value of 400 pS, which is a conservative estimate of the conductance of mammalian cortical electrical coupling (Connors and Long 2004). With these parameter values, we find that changing the location of the coupling can induce interesting alternations in the stability of the sychronous and the anti-phase state. However, the robustness of phase-locking decays rapidly as the position of the electrical coupling is located further away from the somata.

4.1 Existence and stability of phase-locking

Figure 4 plots the bifurcation diagrams of the phase-locked states (upper panels) as a function of the electrotonic length of the dendrite (and therefore the location of the electrical coupling) for different somatic firing frequencies ω and dendritic radii a.

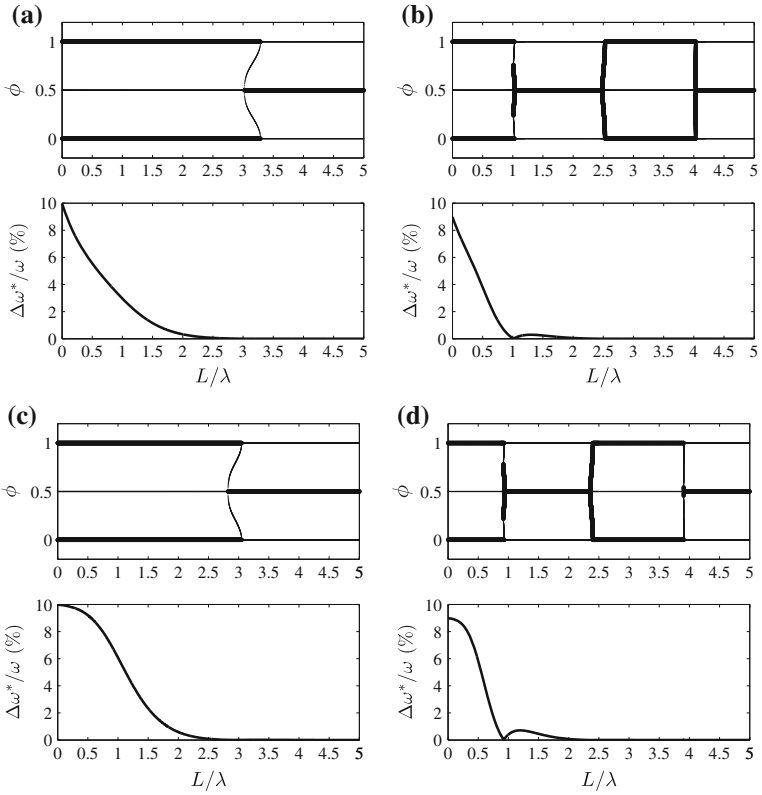

Fig. 4 Stability and robustness of phase-locking to heterogeneity. Stability and robustness of the phase-locked states are plotted as a function of $\frac{L}{\lambda}$ when the conductance of the electrical coupling is 400 pS and the somata are firing at a frequency of 31 Hz (**a**, **c**) and 94 Hz (**b**, **d**). The radius of the dendrite is 0.2 μm in **a** and **b** and 2 μm in **c** and **d**. The *upper panels* plot the stability of the phase-locked solutions of Eq. (19). The stable phase-locked states are plotted as *thick lines* while the unstable states are plotted as *thin lines*. The *lower panels* plot the robustness of the phase-locked states where robustness is measured as the maximum percent frequency heterogeneity the system can tolerate before 1:1 phase-locking is lost, i.e., $\frac{\Delta\omega^*}{\omega}$. For the higher firing frequency, there are more exhanges in stability between the synchronous and anti-phase states as the positions of the electrical synapse is moved further away from the somata. However, for all cases shown, the robustness of phase-locking decays rapidly as $\frac{L}{\lambda}$ is increased

For $\omega = 31$ Hz and $a = 0.2$ μm or $a = 2$ μm as in (a) and (c), when the coupling is between the somata ($\frac{L}{\lambda} = 0$) the synchronous solution is stable while the anti-phase solution is unstable. As $\frac{L}{\lambda}$ increases, a subcritical pitchfork bifurcation occurs and the anti-phase state becomes stable. This is soon followed by an additional subcritical pitchfork bifurcation which causes the synchronous state to become unstable. Thus, there is an exchange of stability between the synchronous and anti-phase solutions with a small region of bistability between these two states. When the firing frequency is 94 Hz and $a = 0.2$ μm or $a = 2$ μm as in Fig. 4b, d, at $\frac{L}{\lambda} = 0$ the synchronous state is stable while the anti-phase state is unstable. As we increase $\frac{L}{\lambda}$, we again get an exchange of stability between the two states, however the first exchange occurs at a lower value of $\frac{L}{\lambda}$ and there are several subsequent exhanges of stability at larger

values of $\frac{L}{\lambda}$. Furthermore, the bifurcations associated with the exchanges of stability are nearly vertical. Note that this alternation of stability between synchrony and anti-phase as the synapse is moved further away from the soma was also found by Crook et al. (1998) in the case of chemical synapses.

4.2 Dendritic filtering and bifurcations of phase-locked states

As the membrane potential of the somata of cell j oscillates, its effects on the dendritic membrane potential propagates through the passive dendrites and gap junction. Different Fourier modes of the membrane potential decay and propagate through the dendrite at different rates, leading to particular attenuation and phase shifts of each mode at the somato-dendritic junction of cell k. By examining these filtering properties of the dendrite, we can understand how the location of the electrical coupling leads to the behavior described in the previous section. As mentioned earlier, the effects of the dendritic filtering and electrical coupling on phase-locking are completely captured by the εc_n terms in the coupling current and, therefore, in $G(\phi)$ (Eq. 19). The definition of c_n (13) reveals the explicit dependence of c_n (and therefore the filtering properties of coupling between the somata) on the nondimensional gap junctional conductance, g, the electrotonic length of the dendrite, $\frac{L}{\lambda}$, and the intrinsic period of the somatic oscillators T. The c_n terms are complex numbers and can be written as

$$c_n\left(g, \frac{L}{\lambda}, \frac{T}{\tau_D}\right) = |c_n| e^{i\psi_n}. \tag{23}$$

$\varepsilon|c_n|$ and ψ_n respectively represent the attenuation factor and phase shift of the nth mode of the somato-dendritic current caused by the dendritic filtering. Note that the attenuation factor scales the amplitude of the nth Fourier mode of the coupling current flowing into cell j resulting from fluctuations of somata k's membrane potential (see Eq. 16).

Using (23), $G(\phi)$ can be rewritten as

$$G(\phi) = \frac{1}{T^2} \sum_{n \neq 0} \varepsilon |c_n| |z_{-n} v_n| e^{i(\xi_n + \psi_n)} [e^{-2\pi i n \phi} - e^{2\pi i n \phi}] \tag{24}$$

$$= \frac{4\varepsilon}{T^2} \sum_{n=1} \varepsilon |c_n| |z_n v_n| \sin(\xi_n + \psi_n) \sin(2\pi n \phi), \tag{25}$$

where ξ_n is the phase shift corresponding to $z_n v_n$, i.e., $z_n v_n = |z_n v_n| e^{i\xi_n}$.

Figure 5 plots the attenuation factor $\varepsilon|c_n|$ and the phase shift ψ_n as a function of $\frac{L}{\lambda}$ and n for different firing frequencies and different dendritic radii. In all cases, the figures reveal that $\varepsilon|c_n|$ decays rapidly with $\frac{L}{\lambda}$ and that this decay is faster for higher n. Furthermore, increasing the firing frequency causes an increase in the attentuation of the higher modes relative to the first mode. Figure 5e, f plots the phase shift of the first mode ψ_1 for the two different firing frequencies, high and low respectively. In both plots, as $\frac{L}{\lambda}$ increases, the magnitude of the phase shift increases monotonically

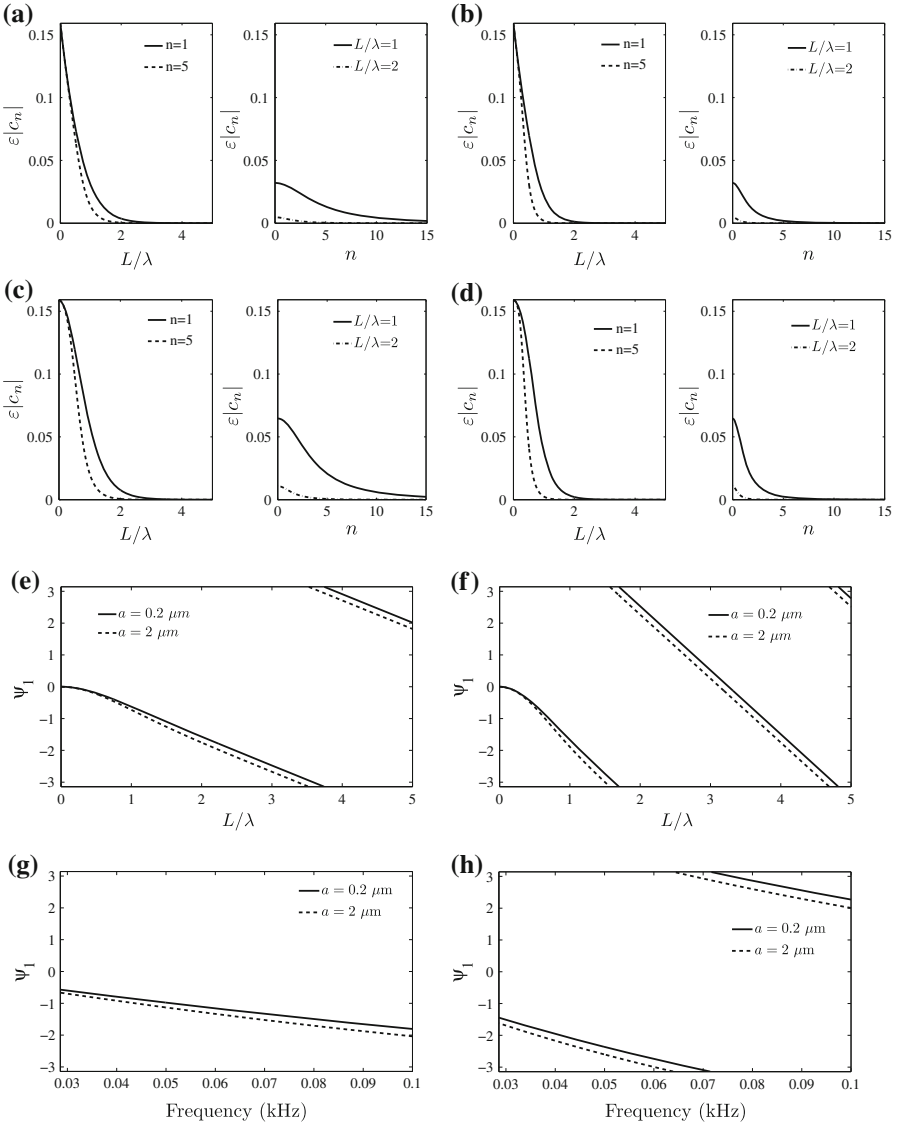

Fig. 5 Dendritic filtering properties. In **a**–**d**, the attenuation factor $\varepsilon|c_n|$ is plotted as a function of $\frac{L}{\lambda}$ (*left panels*) and n (*right panels*). The intrinsic firing frequency is 31 Hz in **a**, **c**, and **e**, and 94 Hz in **b**, **d**, and **f**. The radius of the dendrite is 0.2 μm in **a** and **b**, and 2 μm in **c** and **d**. In the *left hand panels* of **a**–**d**, the *solid lines* plot the $n = 1$ mode of the attenuation factor while the *dashed lines* plot the $n = 5$ mode. Similarly, in the *right hand panels* of each figure, the *solid lines* (*dashed lines*) plot the attenuation factor when $\frac{L}{\lambda} = 1$ ($\frac{L}{\lambda} = 2$). The phase shift factor of the first mode ψ_1 is plotted as a function of $\frac{L}{\lambda}$ when the neuron is firing at a frequency of 31 Hz (**e**) and 94 Hz (**f**) and when the dendritic radius is $a = 0.2$ μm (*solid line*) and $a = 2$ μm (*dashed line*). The phase shift is also plotted as a function of firing frequency for **g** $\frac{L}{\lambda} = 1$ and **h** $\frac{L}{\lambda} = 2$. In all figures, $g_c = 400$ pS. The rapid decay of the attenuation factor with increasing $\frac{L}{\lambda}$ explains the decay in robustness observed in Fig. 4. The periodic nature of the phase-shift causes the exchanges in stability observed in Fig. 4

but the periodic nature of phase shifts makes it an effectively oscillatory function with $\phi_n \in [-\pi, \pi)$. Comparing Fig. 5e, f, one can clearly see that ψ_1 oscillates more rapidly with $\frac{L}{\lambda}$ at higher firing frequencies. Note that the rate of increase of the magnitude of ψ_n also increases as n is increased (not shown). Figure 5g, h plots the phase shift of the first mode as a function of the somatic firing frequency for $\frac{L}{\lambda} = 1$ and $\frac{L}{\lambda} = 2$, respectively. Note that the magnitude of the phase shift is larger for higher firing frequencies. Furthermore, increasing the dendritic length causes the magnitude of the phase shift to increase more rapidly [compare (g) and (h)]. The same qualitative trends occur for higher modes.

It is the periodic oscillations in the phase shifts that are primarily responsible for the exchanges in stability between the synchronous and anti-phase states described in the previous section. To understand why this is the case, it is instructive to examine the dominant ($n = 1$) mode of the expansion of $G(\phi)$. Replacing $G(\phi)$ with its first mode results in the following approximation to (18)

$$\frac{d\phi}{dt} = \frac{1}{\tau_D} G(\phi) \approx \frac{1}{\tau_D} \frac{4}{T^2} \varepsilon |c_1||z_1 v_1| \sin(\xi_1 + \psi_1) \sin(2\pi\phi). \tag{26}$$

This approximate phase model has phase-locked states only at $\phi^* = 0, \frac{1}{2}$, corresponding to synchrony and anti-phase. The stability of the synchronous and anti-phase states are given respectively by the signs of

$$\begin{aligned} G'(0) &\approx \left[\frac{8\pi}{T^2} \varepsilon |c_1||z_1 v_1|\right] \sin(\xi_1 + \psi_1) \\ G'(1/2) &\approx -\left[\frac{8\pi}{T^2} \varepsilon |c_1||z_1 v_1|\right] \sin(\xi_1 + \psi_1). \end{aligned} \tag{27}$$

Thus, the stability of the synchronous and anti-phase states will be determined by the sign of $\sin(\xi_1 + \psi_1(\frac{L}{\lambda}))$. Specifically, as $\psi_1(\frac{L}{\lambda})$ changes with increased $\frac{L}{\lambda}$, the sign of $\sin(\xi_1 + \psi_1(\frac{L}{\lambda}))$ will change periodically inducing a switch in stability of the synchronous and anti-phase states. Furthermore, the switches in stability (bifurcations) will occur when $\xi_1 + \psi_1(\frac{L}{\lambda})$ is equal to an integer multiple of π. When only the first mode ($n = 1$) of $G(\phi)$ is taken into consideration, as in (27), the exchanges of stability will arise from vertical bifurcations, i.e., a degenerate bifurcations where there are instantaneous changes in the stability of various steady-states.

For high firing frequencies, the first mode of $G(\phi)$ is highly dominant (see Fig. 5a–d) resulting in almost vertical bifurcations of steady-states with fast exchanges in stability, as in Fig. 4b, d. For lower firing frequencies, the first mode of $G(\phi)$ is less dominant and including the higher modes of the expansion will result in smoother bifurcations, as in Fig. 4a, c. Note that this implies that additional bifurcations would be observed in Fig. 4 if $\frac{L}{\lambda}$ were increased well-past 5. A similar interpretation of this alternation in stability was given by Crook et al. (1998) for the case of two ball-and-stick neurons coupled with chemical synapses. Note that increasing the dendritic radius to 2 μm (dotted line) causes only a small

leftwards shift of ψ_1 for both firing frequencies (see Fig. 5e, f). This implies that increasing the dendritic radius would cause the switches in stability between synchrony and anti-phase seen in Fig. 4 to occur for only slighly smaller values of $\frac{L}{\lambda}$.

4.3 Robustness of phase-locked states

In this section, we examine the robustness of the phase-locked solutions to heterogeneity. Although prior studies (Bressloff and Coombes 1997; Crook et al. 1998; Lewis and Rinzel 2004; Remme et al. 2009) have examined the effects of dendritic properties on the existence and stability of phase-locking, the robustness of these phase locked states to heterogeneity and/or noise has not been examined explicitly. Because real neural systems are subject to varying amounts of heterogenity and noise, examining the robustness of the phase-locked solutions is of vital importance.

The lower planels in Fig. 4 plot the measure of robustness of the stable phase-locked states as a function of the position of the electrical coupling $\frac{L}{\lambda}$. Recall robustness is measured by the maximum relative frequency difference between the two cells that allows 1:1 phase-locking to occur $\frac{\Delta\omega^*}{\omega}$. When the intrinsic firing frequency is 31 Hz, as in Fig. 4a, c, robustness decays with increasing $\frac{L}{\lambda}$ and is approximately 0.5 % at $\frac{L}{\lambda} = 2$, i.e., robustness is effectively zero well before the bifurcation to stable anti-phase. Increasing the firing frequency as in Fig. 4b, d, causes the robustness to decay more rapidly. Note that $\frac{\Delta\omega^*}{\omega}$ is zero at the points where the synchronous and anti-phase states exchange stability, which is a necessary consequence of there being a bifurcation. After the first bifurcation, there is an increase in robustness of the anti-phase state, however, the robustness never goes far above 0.5 %. Increasing the radius an order of magnitude from 0.2 to 2 μm causes an increase in the robustness (especially at lower values of $\frac{L}{\lambda}$) but this large increase in radius still leads to a small level of robustness at moderate values of $\frac{L}{\lambda}$. The small level of robustness observed in all of the above cases suggests that it is highly unlikely that even a single exchange in the stability of the synchronous and anti-phase states would be observed in real electrically coupled neurons.

Plugging Eq. (25) into Eq. (22), we find that the maximum relative frequency difference before 1:1 phase-locking is lost obeys the following inequality

$$\begin{aligned}
\frac{\Delta\omega^*}{\omega} &= \max_{\phi}\left|\frac{T}{\tau_D}G(\phi)\right| \\
&= \max_{\phi}\left|\frac{4}{T\tau_D}\sum_{n=1}^{\infty}|z_n v_n|\sin\left(\psi_n\left(\frac{L}{\lambda}\right)+\xi_n\right)\varepsilon\left|c_n\left(\frac{L}{\lambda}\right)\right|\right| \\
&\leq \frac{4}{T\tau_D}\sum_{n=1}^{\infty}|z_n v_n|\varepsilon\left|c_n\left(\frac{L}{\lambda}\right)\right| \\
&\leq \varepsilon\left|c_1\left(\frac{L}{\lambda}\right)\right|\left\{\frac{4}{T\tau_D}\sum_{n=1}^{\infty}|z_n v_n|\right\}.
\end{aligned}$$

Thus, the overall rapid decay in the robustness of phase-locked states with increasing $\frac{L}{\lambda}$ (including dependence on dendritic radius and intrinsic somatic firing frequency) can be understood in terms of the attenuation factor of the first mode $\varepsilon \left| c_1 \left(\frac{L}{\lambda}\right)\right|$, as described in the section 4.2. Note, however, that the non-monotonicity in robustness that is observed in Fig. 4b, d can be explained by examining Eq. (26) and recalling the fact that the phase shifts are periodic functions of $\frac{L}{\lambda}$. Thus, the robustness in this case is also affected by the magnitude of the sinusoidal terms $|\sin(\xi_n + \psi_n \left(\frac{L}{\lambda}\right))|$ which will necessarily be zero when there is a shift in stability of the phase-locked states, i.e., at bifurcation points.

5 Re-examining the robustness of phase-locking for fixed coupling coefficient

The results in Sect. 4 suggest that the phase-locking of electrically coupled neurons with dendritic structure is extremely fragile to heterogeneity when the coupling is located beyond proximal dendrites. Furthermore, in Sect. 7, we will show that qualitatively similar results hold when considering robustness to weak somatic noise. Thus, given the high level of heterogeneity and noise in real neural systems, it would appear that phase-locking between neurons with distal electrical coupling is unlikely to be observed. However, note that we used a fixed coupling conductance $g_c = 400$ pS which comes from estimates in previous studies, (e.g Amitai et al. 2004; Beierleinet al. 2000; Gibson et al. 1999; Connors and Long 2004). These studies use single-compartment models to estimate g_c from the experimentally measured coupling coefficient (CC). By neglecting the spatial properties of the neurons, the estimates resulting from this model will substantially underestimate g_c for coupling on distal dendrites (Prinz and Fromherz 2002). This, in turn, could substantially affect the estimates of the robustness of phase-locking. To address this issue, we re-examine the dependence of phase-locking on $\frac{L}{\lambda}$ using a fixed CC and using ball-and-stick model neurons to derive an estimate of g_c from the coupling coefficient. In particular, we use a value of $CC = 0.05$ which is in the range of values measured for putative electrical coupling on distal dendrites between cortical inhibitory neurons (Amitai et al. 2004).

5.1 Properties of the coupling coefficient

The CC between cell 1 and cell 2 is measured by injecting a current in cell 1 and measuring the change in potential for both cells that results from this current injection, i.e., ΔV_1 and ΔV_2. The CC is then given by

$$CC = \frac{\Delta V_2}{\Delta V_1}. \tag{28}$$

By assuming each cell is a single passive compartment, it can be shown that

$$g_c = \pi d^2 g_L \frac{CC}{1 - CC}, \tag{29}$$

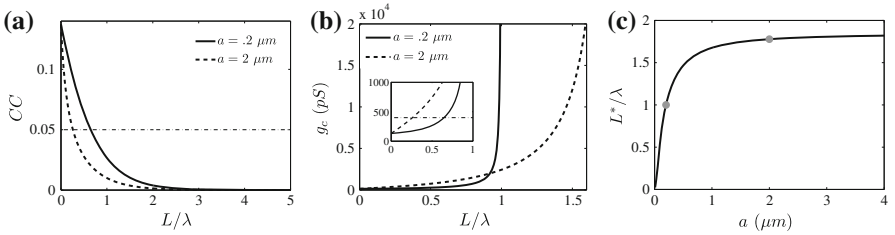

Fig. 6 Coupling coefficient of the ball-and-stick model. **a** Coupling coefficient as a function of $\frac{L}{\lambda}$ when $g_c = 400$ pS and the dendritic radius is 0.2 μm (*solid line*) or 2 μm (*dashed line*). For reference, the *dash-dotted line* plots the value $CC = 0.05$ we use in our analysis. The coupling coefficient decays as the coupling is positioned further way from the cell bodies and the rate of this decay is increased as the dendritic radius is increased. **b** Electrical synaptic conductance estimated using the CC as a function of $\frac{L}{\lambda}$ when $CC = 0.05$. Again for reference the *inset* is a blow up of the region $\frac{L}{\lambda} \in [0, 1]$ and the the *dash-dotted line* plots $g_c = 400$ pS which is the value we used in the previous section. To maintain a fixed CC the gap junctional conductance must increase as $\frac{L}{\lambda}$ is increased. **c** Maximum distance the electrical synapse can be located away from the cell bodies $\frac{L^*}{\lambda}$ as a function of dendritic radius a. The two *solid gray circles* highlight the values $a = 0.2$ μm and $a = 2$ μm which are the dendritic radius values we utilize in our analysis

where d is the diameter of each compartment and g_L is the resting membrane conductance (Bennett 1977). Estimating g_c in this manner omits the effect of dendritic filtering. The value of the coupling coefficient for two identical electrically-coupled-ball-and-stick neurons was derived by Prinz and Fromherz (2002). In the Appendix B we present an alternate derivation that allows for heterogeneity in the dendritic parameters of the two neurons. For the case of identical neurons

$$CC = \frac{2\varepsilon g_{LD} g}{g_L + \sinh\left(2\frac{L}{\lambda}\right)[\varepsilon g_{LD} + 2g_L g] + \cosh\left(2\frac{L}{\lambda}\right)[2\varepsilon g_{LD} g + g_L]}. \tag{30}$$

Figure 6a plots CC as a function of $\frac{L}{\lambda}$ for $g_c = 400$ pS. Note that CC decays with increasing $\frac{L}{\lambda}$, and the rate of this decay is increased as the dendritic radius a is increased. Using (30) the electrical coupling conductance can be estimated for a fixed value of CC

$$\begin{aligned} g_c &= \gamma \frac{CC}{1 - \alpha CC} \\ \gamma &= \frac{\pi a^2}{R_i \lambda 2\varepsilon g_{LD}} \left[g_L + \varepsilon g_{LD} \sinh\left(2\frac{L}{\lambda}\right) + g_L \cosh\left(2\frac{L}{\lambda}\right) \right] \\ \alpha &= \left[\frac{g_L}{\varepsilon g_{LD}} \sinh\left(2\frac{L}{\lambda}\right) + \cosh\left(2\frac{L}{\lambda}\right) \right]. \end{aligned} \tag{31}$$

Note that Eq. (31) limits to (29) as $\frac{L}{\lambda} \to 0$. Equation (31) shows that g_c is an increasing function of $\frac{L}{\lambda}$ until a discontinuity is reached at

$$\frac{L^*}{\lambda} = \frac{i}{2}\left(\sin^{-1}\left(\frac{\varepsilon g_{LD}}{CC}\frac{1}{\sqrt{(\varepsilon g_{LD})^2 - g_L^2}}\right) - \tan^{-1}\left(\frac{(\varepsilon g_{LD})^2}{g_L i}\right)\right). \quad (32)$$

Note that the right hand side of the above equation is a real number. $2\frac{L^*}{\lambda}$ can be interpreted as the electrotonic length of a single dendrite that connects the two somata and yields a particular coupling coefficient of CC. Figure 6b plots g_c as a function of $\frac{L}{\lambda}$ for $CC = 0.05$. Figure 6c shows that, for a fixed value of $CC = 0.05$, the maximum distance that the electrical coupling can be located away from the somata, $\frac{L^*}{\lambda}$, increases as the dendritic radius is increased but eventually saturates. Thus, fixing the coupling coefficient imposes a maximal distance that the electrical coupling can be located from the somata.

5.2 Existence, stability, and robustness re-visited

We now examine how dendritic properties and electrical coupling affect the existence, stability, and robustness of phase-locking for a fixed $CC = 0.05$ when the coupling conductance value is calculated using (31). Note that $g_c = 400$ pS would yield a $CC = 0.14$ when $\frac{L}{\lambda} = 0$ and a $CC = 0.027$ when $\frac{L}{\lambda} = 1$ and $a = 0.2$ μ m. From these values we expect that, when the coupling is between the somata or proximal dendrites, the phase-locked states from the previous analysis with fixed $g_c = 400$ pS will have greater robustness than phase-locked states for a fixed $CC = 0.05$. On the other hand, when the coupling is located on distal dendrites, phase-locked states with a fixed $CC = 0.05$ will have greater robustness than those for fixed $g_c = 400$ pS.

Similar to Fig. 4, Fig. 7 plots the bifurcation diagrams of the phase-locked states and their robustness as a function of the location of the electrical coupling for different somatic firing frequencies and different dendritic radii. Note that, because of the fixed CC, $\frac{L}{\lambda}$ in Fig. 7 cannot be increased beyond $\frac{L^*}{\lambda}$. As a result of this limitation on $\frac{L}{\lambda}$, only the synchronous solution is stable for all parameters shown except for when the firing frequency is high ($\omega = 94$ Hz) and the dendritic radius is large ($a = 2$ μm), in which case there is only a single exchange in stability between the synchronous and anti-phase solutions rather than multiple exchanges as seen in Fig. 4. Consistent with our expectations, the lower panels in Fig. 7 show that the phase-locked states for a fixed $CC = 0.05$ (solid black lines) are less robust at lower values of $\frac{L}{\lambda}$ and are more robust at higher values of $\frac{L}{\lambda}$ than the corresponding phase-locked states for a fixed $g_c = 400$ pS (solid gray lines). Interestingly, in all cases shown for a fixed CC, robustness *increases* with increasing $\frac{L}{\lambda}$ at least for small values of $\frac{L}{\lambda}$.

As was the case for fixed g_c, the bifurcation scenarios and the associated robustness of the phase-locked states for fixed CC can be understood in terms of the filtering properties of the dendrites. The lack of exchanges in stability between the synchronous and anti-phase states arises from the limited changes in the phase shifts ψ_n as $\frac{L}{\lambda}$ is increased (Fig. 8e, f). The robustness results described above can be explained by the variation of the attenuation factors $\varepsilon|c_n|$ with $\frac{L}{\lambda}$. Specifically, $\varepsilon|c_n|$ show an increase with $\frac{L}{\lambda}$ at small values of $\frac{L}{\lambda}$ and are relatively high for large values of $\frac{L}{\lambda}$ compared to those for fixed g_c (Fig. 8a–d). This results from the fact that when CC is fixed,

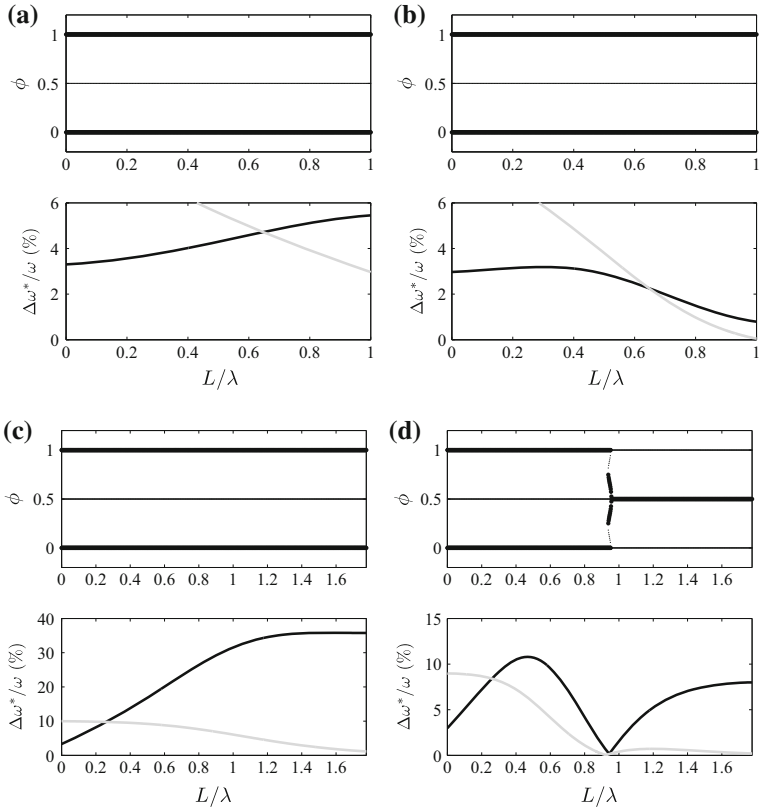

Fig. 7 Stability and robustness phase-locking to heterogeneity for a fixed coupling coefficient. Stability and robustness of the phase-locked states are plotted as a function of $\frac{L}{\lambda} \in [0, \frac{L^*}{\lambda}]$ when the coupling coefficient is fixed at $CC = 0.05$ and the somata are firing at a frequency of 31 Hz (**a**, **c**) and 94 Hz (**b**, **d**). The radius of the dendrite is 0.2 μm in **a** and **b** and 2 μm in **c** and **d**. The *upper panels* plot the stability of the phase-locked solutions of equation (19). The stable phase-locked states are plotted as *thick lines* while the unstable states are plotted as *thin lines*. The *lower panels* plot the robustness of the phase-locked states where robustness is measured as the maximum percent frequency heterogeneity the system can tolerate before 1:1 phase-locking is lost, i.e., $\frac{\Delta\omega^*}{\omega}$. For reference, the robustness of the corresponding phase-locked states when $g_c = 400$ pS is plotted as the light gray curves (see Fig. 4). Fixing CC causes fewer exchanges in stability as $\frac{L}{\lambda}$ is increased, and it also causes the phase-locked states to be more robust than those for a fixed g_c

g_c increases with increasing $\frac{L}{\lambda}$, according to equation (31) and seen in Fig. 6b. Note that, with all other explicit parameters in the model held constant, the attenuation factors decrease with increases in $\frac{L}{\lambda}$ and increase with increases in the coupling conductance g_c. Thus, for fixed CC, when $\frac{L}{\lambda}$ is increased and there is a corresponding increase in g_c, the attentuation factors can increase with $\frac{L}{\lambda}$ or have a non-monotonic dependence as observed in Fig. 8.

Figure 9 demonstrates that the previous observations regarding the robustness of phase-locking for fixed g_c and fixed CC carry over to a wide range of somatic firing frequencies. Specifically, Fig. 9a, d show that phase-locked states are *more* robust for

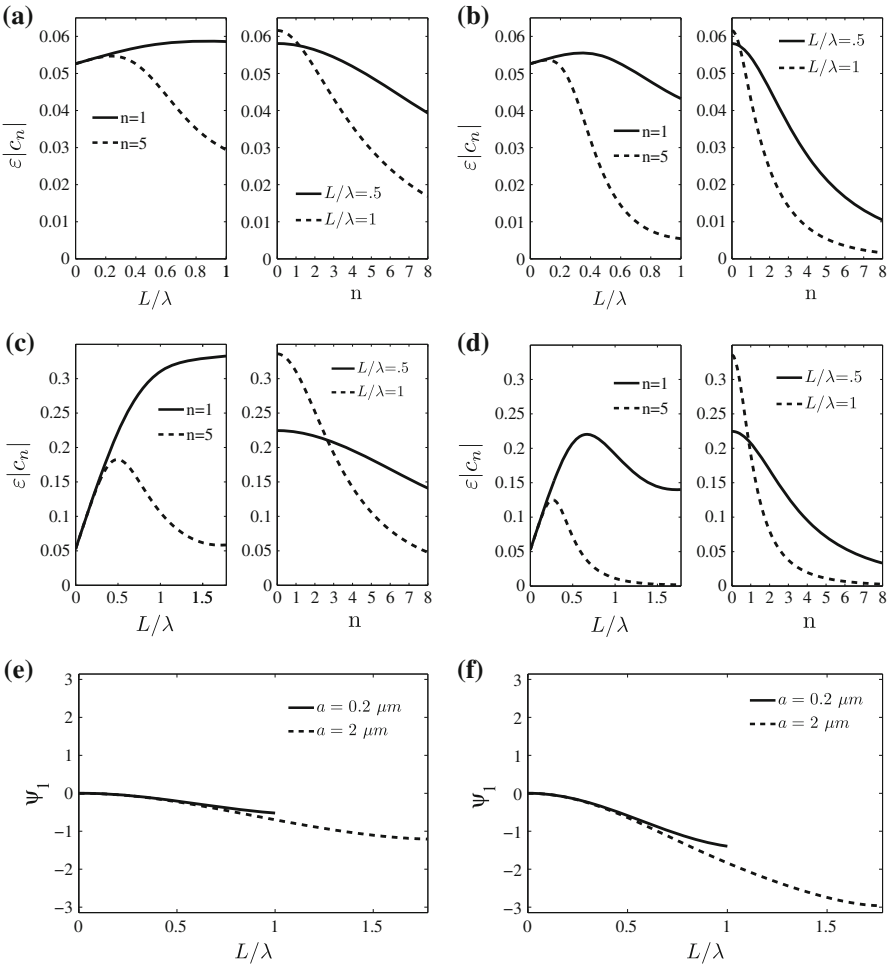

Fig. 8 Dendritic filtering properties for a fixed coupling coefficient. In **a**–**d**, the attenuation factor $\varepsilon|c_n|$ is plotted as a function of $\frac{L}{\lambda} \in [0, \frac{L^*}{\lambda}]$ (*left panels*) and n (*right panels*). The intrinsic firing frequency is 31 Hz in **a**, **c**, and **e**, and 94 Hz in **b**, **d**, and **f**. The radius of the dendrite is 0.2 μm in **a** and **b**, and 2 μm in **c** and **d**. In the *left hand panels* of **a**–**d**, the *solid lines* plot the $n = 1$ mode of the attenuation factor while the *dashed lines* plot the $n = 5$ mode. Similarly, in the *right hand panels* of each figure, the *solid lines* (*dashed lines*) plot the attenuation factor when $\frac{L}{\lambda} = 1$ ($\frac{L}{\lambda} = 2$). The phase shift factor of the first mode ψ_1 is plotted as a function of $\frac{L}{\lambda}$ when the neuron is firing at a frequency of 31 Hz (**e**) and 94 Hz (**f**) and when the dendritic radius is $a = 0.2$ μm (*solid line*) and $a = 2$ μm (*dashed line*). In all figures, $CC = 0.05$. Fixing CC causes g_c to increase with $\frac{L}{\lambda}$. This causes the magnitude of the phase-shift for fixed CC to increase more slowly with $\frac{L}{\lambda}$ than the case of a fixed g_c. This leads to fewer exchanges in stability of phase-locked states for the case of a fixed CC. It also causes the attenuation factors to sometimes have a non-monotonic dependence on $\frac{L}{\lambda}$

fixed $g_c = 400$ pS ($CC = 0.14$) than for fixed $CC = 0.05$ ($g_c = 170$ pS) when the coupling is between the somata, i.e., $\frac{L}{\lambda} = 0$. On the other hand, when $\frac{L}{\lambda} = 1$ and $a = 0.2\ \mu m$, Fig. 9b, d show that phase-locked states are *less* robust for fixed

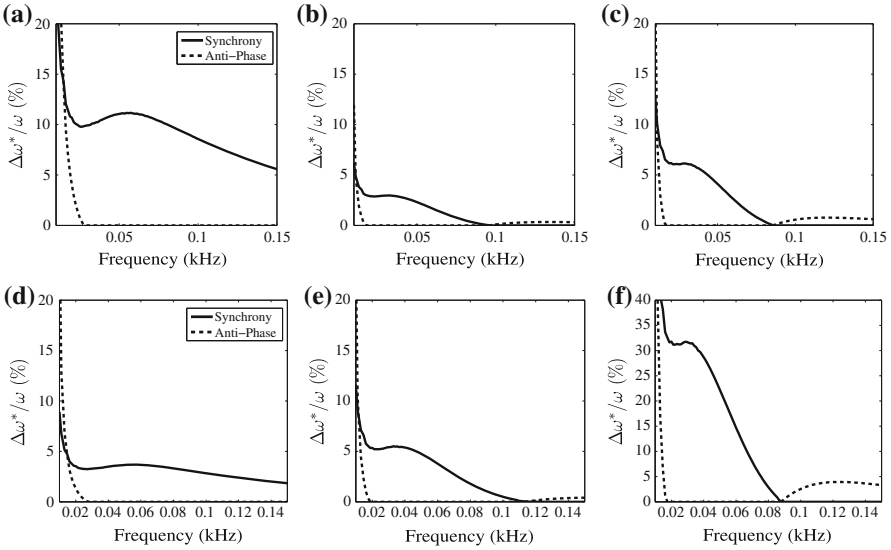

Fig. 9 Comparison of the robustness of phase-locking to heterogeneity as firing frequency is varied for a fixed g_c and a Fixed CC. Robustness of the phase-locked states is plotted as a function of firing frequency when the electrical coupling conductance is held constant at 400 pS (**a**–**c**) and when the coupling coefficient is held constant at 0.05 (**d**–**f**). In **a** and **d**, the dendritic length ($\frac{L}{\lambda}$) is equal to zero while in **b**, **c**, **e** and **f** $\frac{L}{\lambda} = 1$. The dendritic radius is 0.2 μm in **b** and **e** and 2 μm in **c** and **f**. Note the difference in the *y-axis* scale for **f**. For all firing frequencies, fixing CC results in more robust phase-locking for distally located electrical synapses than for a fixed g_c

$g_c = 400$ pS ($CC = 0.027$) than for fixed $CC = 0.05$ (g_c effectively infinite). Similarly, when $\frac{L}{\lambda} = 1$ and $a = 2$ μ m, Fig. 9c, e again show that phase-locked states are less robust for fixed $g_c = 400$ pS ($CC = 0.01$) than for fixed $CC = 0.05$ ($g_c = 2430$ pS).

6 The effects of dendritic heterogeneity

The previous sections have considered heterogeneity between the somatic dynamics. However, heterogeneity can also exist in the dendrites of the two neurons. In this section we consider two natural sources of heterogeneity: the electrotonic lengths of the dendrites of the two neurons, and the leakage channel reversal potentials. Including these dendritic heterogeneities in the nondimensional coupled ball-and-stick model (5) yields

$$\begin{cases} \frac{\partial V_j}{\partial \bar{t}} = \frac{\partial^2 V_j}{\partial \bar{x}^2} - (V_j - \overline{E}^j_{LD}) \\ \frac{\partial V_j}{\partial \bar{t}}(0,\bar{t}) = -\overline{I}_{ion,S}(V_j(0,\bar{t}),\vec{w}) + \overline{I} + \varepsilon \frac{\partial V_j}{\partial \bar{x}}(0,\bar{t}) \\ \frac{\partial V_j}{\partial \bar{x}}\left(\frac{L_j}{\lambda},\bar{t}\right) = g\left(V_k\left(\frac{L_k}{\lambda},\bar{t}\right) - V_j\left(\frac{L_j}{\lambda},\bar{t}\right)\right), \end{cases} \tag{33}$$

where $\frac{L_j}{\lambda}$ is the electrotonic length of the dendrite of the jth neuron, and $\overline{E}_{LD}^{j}$ is the nondimensional dendritic leakage reversal potential of the jth neuron. Approximating the solution of above system as in Sect. 3.1 yields

$$\begin{aligned} V_j(\overline{x},\bar{t},\overline{T}\phi_j,\overline{T}\phi_k) = &\left[\left(\frac{V_0}{\overline{T}}-\overline{E}_{LD}^{k}\right)c_0^{jk}+\left(\frac{V_0}{\overline{T}}-\overline{E}_{LD}^{j}\right)d_0^{jk}+(\overline{E}_{LD}^{k}-\overline{E}_{LD}^{j})f^{jk}\right]\sinh(\overline{x}) \\ &+\left(\frac{V_0}{\overline{T}}-\overline{E}_{LD}^{j}\right)\cosh(\overline{x})+\frac{1}{\overline{T}}\sum_{n\neq 0}\left[V_n\left(\frac{1}{b_n}c_n^{jk}e^{2\pi in\overline{T}\phi_k/\overline{T}}\right.\right. \\ &\left.\left.+\frac{1}{b_n}d_n^{jk}e^{2\pi in\overline{T}\phi_j/\overline{T}}\right)\sinh(b_n\overline{x})+V_n e^{2\pi in\overline{T}\phi_j/\overline{T}}\cosh(b_n\overline{x})\right]e^{2\pi in\bar{t}/\overline{T}} \\ &+\overline{E}_{LD}^{j} \end{aligned} \tag{34}$$

where $b_n=\sqrt{1+2\pi in/\overline{T}}$ and

$$c_n^{jk}=\frac{g}{\cosh\left(b_n\frac{L_j}{\lambda}\right)}\frac{1}{\cosh\left(b_n\frac{L_k}{\lambda}\right)+\frac{g}{b_n}\tanh\left(b_n\frac{L_j}{\lambda}\right)\cosh\left(b_n\frac{L_k}{\lambda}\right)+\frac{g}{b_n}\sinh\left(b_n\frac{L_k}{\lambda}\right)} \tag{35}$$

$$d_n^{jk}=-b_n\frac{\sinh\left(b_n\left(\frac{L_j+L_k}{\lambda}\right)\right)+\sinh\left(b_n\left(\frac{L_j-L_k}{\lambda}\right)\right)+2\frac{g}{b_n}\cosh\left(b_n\left(\frac{L_j+L_k}{\lambda}\right)\right)}{\cosh\left(b_n\left(\frac{L_j+L_k}{\lambda}\right)\right)+\cosh\left(b_n\left(\frac{L_j-L_k}{\lambda}\right)\right)+2\frac{g}{b_n}\sinh\left(b_n\left(\frac{L_j+L_k}{\lambda}\right)\right)} \tag{36}$$

$$f^{jk}=\frac{g}{\cosh\left(\frac{L_j}{\lambda}\right)+g\sinh\left(\frac{L_j}{\lambda}\right)+g\cosh\left(\frac{L_j}{\lambda}\right)\tanh\left(\frac{L_k}{\lambda}\right)} \tag{37}$$

Thus, the phase model in dimensional form is given by

$$\begin{aligned} \frac{d\phi_j}{dt} &= \frac{1}{\tau_D}\left(\nu_j+\frac{1}{T^2}\sum_{n\neq 0}\left[\varepsilon c_n^{jk}z_{-n}v_n e^{2\pi in(\phi_k-\phi_j)}\right]\right) \\ &= \frac{1}{\tau_D}\left(\nu_j+H_{het}(\phi_k-\phi_j)\right), \end{aligned} \tag{38}$$

where

$$\begin{aligned} \nu_j = &\langle z\rangle\left[\left(\langle v\rangle-E_{LD}^{k}\right)\varepsilon c_0^{jk}+\left(\langle v\rangle-E_{LD}^{j}\right)\varepsilon d_0^{jk}+(E_{LD}^{k}-E_{LD}^{j})\varepsilon f^{jk}\right] \\ &+\frac{1}{T^2}\sum_{n\neq 0}\varepsilon d_n^{jk}z_{-n}v_n. \end{aligned} \tag{39}$$

Letting $\phi = \phi_k - \phi_j$,

$$\begin{aligned}\frac{d\phi}{dt} &= \frac{1}{\tau_D}\left(\nu_k - \nu_j + H_{het}(-\phi) - H_{het}(\phi)\right)\\ &= \frac{1}{\tau_D}\left(\Delta\nu + \frac{1}{T^2}\sum_{n\neq 0}\left\{z_{-n}v_n\varepsilon\left(c_n^{kj}e^{-2\pi in\phi} - c_n^{jk}e^{2\pi in\phi}\right)\right\}\right)\\ &= \frac{1}{\tau_D}G_{het}(\phi),\end{aligned} \tag{40}$$

where

$$\begin{aligned}\Delta\nu = \varepsilon\langle z\rangle\Big[&\left(\langle v\rangle - E_{LD}^j\right)(c_0^{kj} - d_0^{jk}) + \left(\langle v\rangle - E_{LD}^k\right)(d_0^{kj} - c_0^{jk})\\ &+\left(E_{LD}^j - E_{LD}^k\right)(f^{kj} + f^{jk})\Big] + \frac{1}{T^2}\sum_{n\neq 0} z_{-n}v_n\varepsilon(d_n^{kj} - d_n^{jk})\end{aligned} \tag{41}$$

As before, heterogeneity in the somatic firing frequency can be included in the phase model (40) resulting in

$$\frac{d\phi}{dt} = \Delta\omega + \frac{1}{\tau_D}G_{het}(\phi). \tag{42}$$

This phase model allows us to now probe how the additional dendritic heterogeneities affect the stability and robustness of phase-locking.

The dendritic heterogeneities will cause asymmetry in the coupling coefficient. We denote the directional CC measured when the current is injected into cell j and the change in potential of cell k is divided by the change in potential of cell j as

$$CC_k = \frac{\Delta V_k}{\Delta V_j} = \frac{\frac{g_{LD}}{g_L}\varepsilon\frac{g}{\lambda}\rho\left(-\gamma_j\beta_j + \alpha_j\cosh\left(\frac{L_j}{\lambda}\right)\right)}{\frac{g_{LD}}{g_L}\varepsilon\rho\left(\left(\frac{g}{\lambda}\right)^2\gamma_k\cosh\left(\frac{L_j}{\lambda}\right) - \alpha_k\beta_j\right) + 1}, \tag{43}$$

where

$$\begin{aligned}\rho &= \frac{1}{\alpha_k\alpha_j - \left(\frac{g}{\lambda}\right)^2\gamma_k\gamma_j}\\ \alpha_j &= \left[\frac{1}{\lambda} + \frac{g_{LD}}{g_L}\frac{\varepsilon g}{\lambda}\right]\cosh\left(\frac{L_j}{\lambda}\right) + \left[\frac{g}{\lambda} + \frac{g_{LD}}{g_L}\frac{\varepsilon}{\lambda}\right]\sinh\left(\frac{L_j}{\lambda}\right)\\ \beta_j &= \frac{1}{\lambda}\sinh\left(\frac{L_j}{\lambda}\right) + \frac{g}{\lambda}\cosh\left(\frac{L_j}{\lambda}\right)\\ \gamma_j &= \sinh\left(\frac{L_j}{\lambda}\right) + \frac{g_{LD}}{g_L}\varepsilon\cosh\left(\frac{L_j}{\lambda}\right).\end{aligned}$$

The details of this calculation are provided in the Appendix B. Except for the case of $\frac{L_j}{\lambda} = \frac{L_k}{\lambda}$, there is no simple closed form for the coupling conductance estimated from fixed CC_k. Thus, we will use Eq. (43) to numerically solve for g_c when the coupling coefficient for neuron k is fixed. Note that by ensuring that CC_k is fixed, CC_j will still vary with system parameters.

6.1 Asymmetry in dendritic length

Here we explore the effect of asymmetric dendrites on the existence, stability, and robustness of phase-locking. We denote the position of the electrical coupling between the dendrites of the two ball-and-stick neurons by

$$\beta = \frac{L_1}{L_1 + L_2}. \tag{44}$$

In our calculations, we set the total length of the dendrites $\frac{L_1}{\lambda} + \frac{L_2}{\lambda} = 1.5$. For this combined length and symmetric dendrites ($\beta = \frac{1}{2}$), a coupling coefficient $CC_1 = CC_2 = 0.05$ approximately corresponds to a conductance $g_c = 400$ pS. That is, when $\beta = \frac{1}{2}$, the stability and robustness of phase-locking for fixed CC and fixed g_c are similar. We also set $E^1_{LD} = E^2_{LD} = -70$ mV, but note that similar results are obtained when heterogeneity in E_{LD} is considered.

Figure 10 plots the bifurcation diagrams and corresponding robustness for the phase-locked state as a function of the coupling position β when the neurons are firing at a frequency of 31 Hz. The coupling conductance is held fixed, $g_c = 400$ pS, in (a) and (b), while the coupling coefficient $CC_1 = 0.05$ is held constant in (c) and (d). The figure shows that fixed $CC_1 = 0.05$ preserves 1:1 phase-locking more effectively than fixed $g_c = 400$ pS with changes in the coupling position and/or changes in heterogenity in intrinsic firing frequency. However, it can be seen that the existence of 1:1 phase-locking is fragile to changes in the coupling position. This is particularly true for the larger dendritic radius where even small asymmetries in dendritic length completely annhilate the 1:1 phase-locked state. In fact, for all cases shown, dendro-somatic coupling $\beta = 0, 1$ never supports 1:1 phase-locking.

7 Robustness to weak somatic noise

To further explore robustness of phase-locked states, we examine the situation in which the somata are also receiving small amplitude white noise current inputs. The addition of the white noise inputs to the somata results in additive noise in the phase equations (Kuramoto 1984; Pfeuty et al. 2005). We now outline the steps to obtain the steady-state probability density of the phase-difference between two coupled oscillators $\rho_{ss}(\phi)$ (Kuramoto 1984; Pfeuty et al. 2005).

First, if small amplitude independent white noise current is applied to the somata in the electrically coupled ball-and-stick model, the resulting nondimensional model

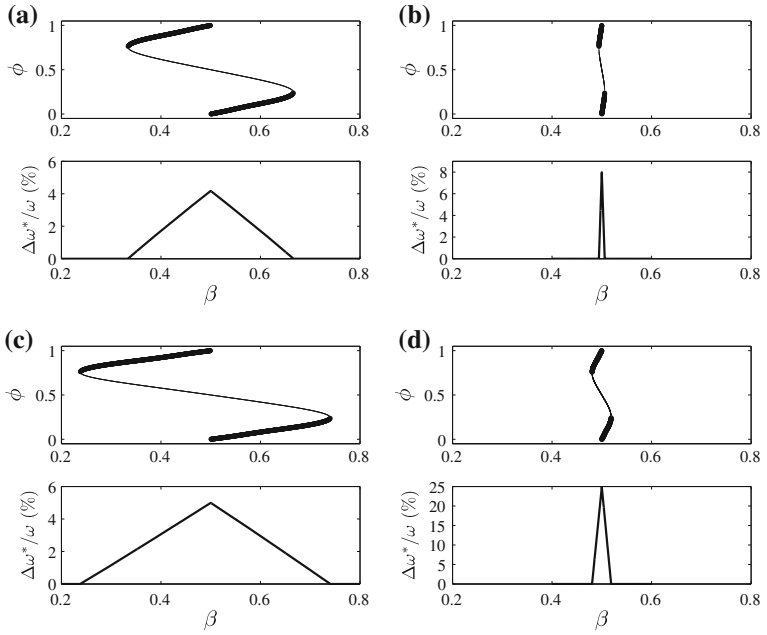

Fig. 10 Effect of changing coupling position on stability and robustness to heterogeneity of phase-locking. The stability (*upper plots*) and robustness (*lower plots*) of phase-locking is plotted as a function of the coupling position for asymmetric dendrites β when the somata are firing at a frequency of 31 Hz. In **a** and **b** the coupling conductance is fixed at $g_c = 400$ pS. In **c** and **d** the directional coupling coefficient for cell 1 fixed at $CC_1 = 0.05$. The dendritic radius is $a = 0.2$ μm in **a** and **c** and $a = 2$ μm in **b** and **d**. The sum of the electronic lengths of the two dendrites is fixed at $\frac{L_1}{\lambda} + \frac{L_2}{\lambda} = 1.5$. Note that 1:1 phase-locking is fragile to changes in the position of the electrical coupling, especially for larger dendritic radii

equations would be

$$\begin{cases} \frac{\partial V_j}{\partial \bar{t}} = \frac{\partial^2 V_j}{\partial \bar{x}^2} - (V_j - \overline{E}_{LD}) \\ \frac{\partial V_j}{\partial \bar{t}}(0,\bar{t}) = -\overline{I}_{ion,S}(V_j(0,\bar{t}),\vec{w}) + \overline{I} + \varepsilon \frac{\partial V_j}{\partial \bar{x}}(0,\bar{t}) + \sigma \overline{\xi}_j(\bar{t}) \\ \frac{\partial V_j}{\partial \bar{x}}\left(\frac{L}{\lambda},\bar{t}\right) = g\left(V_k\left(\frac{L}{\lambda},\bar{t}\right) - V_j\left(\frac{L}{\lambda},\bar{t}\right)\right), \end{cases} \tag{45}$$

where σ^2 is $\mathcal{O}(\varepsilon)$. The term $\overline{\xi}_j(\bar{t})$ represents Gaussian white noise with zero mean and unit variance (i.e., $\langle \overline{\xi}_j(\bar{t}) \rangle = 0$ and $\langle \overline{\xi}_j(\bar{t}) \overline{\xi}_j(\bar{t}') \rangle = \delta(\bar{t} - \bar{t}')$). Performing the phase reduction for this system as in Sect. 3.1 yields the dimensional phase equation (Teramae et al. 2009; Teramae and Tanaka 2004)

$$\frac{d\phi_j}{dt} = \frac{1}{\tau_D} H(\phi_k - \phi_j) + \frac{\sigma}{\sqrt{\tau_D}} s_\phi \xi_j(t), \tag{46}$$

where $\xi_j(t) = \overline{\xi}_j(\tau_D \bar{t})$ and the term $s_\phi = \left(\frac{1}{T}\int_0^T [-E_L z(\tilde{t})]^2 d\tilde{t}\right)^{1/2}$ comes from averaging the noisy phase equations (Kuramoto 1984; Pfeuty et al. 2005). If we now

let $\phi = \phi_2 - \phi_1$, we arrive at

$$\frac{d\phi}{dt} = \frac{1}{\tau_D} G(\phi) + \frac{\sigma}{\sqrt{\tau_D}} s_\phi \sqrt{2}\eta(t), \tag{47}$$

where $G(\phi) = H(-\phi) - H(\phi)$, $\sqrt{2}\eta(t) = \xi_2(t) - \xi_1(t)$, and $\eta(t)$ is also Gaussian white noise with zero mean and unit variance.

The non-linear Langevin equation (47) corresponds to the following Fokker–Planck equation Risken (1989); Stratonovich (1967); van Kampen (1981)

$$\frac{\partial \rho}{\partial t}(\phi, t) = -\frac{\partial}{\partial \phi}\left[\frac{\varepsilon}{\tau_D}\bar{G}(\phi)\rho(\phi, t)\right] + \left(\frac{\sigma s_\phi}{\sqrt{\tau_D}}\right)^2 \frac{\partial^2 \rho}{\partial \phi^2}(\phi, t), \tag{48}$$

where $\varepsilon\bar{G}(\phi) = G(\phi)$ (see Eq. 19), and $\rho(\phi, t)\Delta\phi$ is the probability that the neurons will have a phase difference that is in the interval $(\phi, \phi + \Delta\phi)$ at time t for small $\Delta\phi$. The steady-state density $\left(\frac{\partial \rho}{\partial t} = 0\right)$ is

$$\rho(\phi) = \frac{e^{M(\phi)}}{\int_0^T e^{-M(\bar{\phi})}}, \tag{49}$$

where

$$M(\phi) = \frac{\varepsilon}{(\sigma s_\phi)^2} \int_0^\phi \bar{G}(\bar{\phi}) d\bar{\phi}, \tag{50}$$

where $\frac{\varepsilon}{(\sigma s_\phi)^2}$ represents the ratio of the strength of the dendritic perturbation to the variance of the noise in the soma. Pfeuty et al. (2005) showed that spike-train cross-correlogram of the two neurons is equivalent to this steady-state density (49) for small ε.

The steady-state density $\rho(\phi)$ can be used to examine how dendritic properties affect phase-locking dynamics in the presence of background noise. Because the noise comes in additively, the stable steady-state phase differences of the noiseless system will correspond to peaks in the steady-state density function. Figure 11 plots $\rho_{ss}(\phi)$ for the example G function from Fig. 3. It can clearly be seen that the density has a peak around $\phi = 0$ corresponding to stable synchrony in the noiseless system. Increasing the strength of the noise σ acts to smear out the density function. As the noise increases, the density approaches the uniform distribution for which all phase differences are equally likely. A strongly peaked density function indicates that the phase-locked state is robust to background noise. To quantify the robustness of the phase-locked states to noise, we use the so-called Kuramoto index (Kuramoto 1984):

$$R_n = \left| \int_0^1 \rho_{ss}(\phi) e^{2\pi i \phi} d\phi \right|. \tag{51}$$

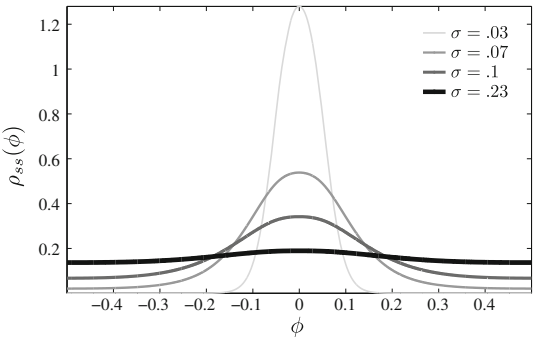

Fig. 11 Phase-locking in the presence of noise. The figure plots an example cross-correlogram (steady-state phase difference density) between the phases of the two cells with varying levels of somatic noise strength σ for the example G function from Fig. 3. A more peaked cross-correlogram for a given noise level, σ, indicates a more robust phase-locked state

$R_n = 1$ corresponds to precise phase-locking, i.e., $\rho_{ss}(\phi) = \delta(\phi - \phi^{ss})$ a delta-function density centered at a phase-locked state of the deterministic system; while $R_n = 0$ corresponds to the phases being uniformly distributed. In all subsequent figures, σ is chosen so that $\frac{T}{\tau_D}\left(\sigma s_\phi\right)^2 = 0.01$, i.e., the noise level can only cause a maximum of 1 % change in the average frequency. This is chosen to illustrate the fact that even in the presence of very small noise, dendritic properties can have large effects on robustness.

Figure 12 plots the stability and robustness of phase-locking to noise for a fixed $g_c = 400$ pS at various firing frequencies and denritic radii. The bifurcation diagrams (top panels) are for the noiseless system which are exactly the same as Fig. 4. The solid curves correspond to peaks of $\rho_{ss}(\phi)$. Similar to Fig. 4, Fig. 12 reveals that, for a fixed g_c, the robustness of phase-locking to noise decays rapidly to zero as the position of the electrical coupling is moved further away from the cell bodies. In particular, for firing frequencies of 31 Hz and 94 Hz and dendritic radii of 0.2 and 2 μm, the Kuramoto index R_n is less than 0.2 for values of $\frac{L}{\lambda} \geq 2$. Note that the system undergoes at most one exchange in stability before significant robustness is lost. Figure 13 plots the stability and robustness of phase-locking to noise for a fixed $CC = 0.05$ for the same firing frequencies and dendritic radii. Similar to Fig. 7, the figure shows that the phase-locked states for a fixed $CC = 0.05$ are less robust at lower values of $\frac{L}{\lambda}$ and are more robust at higher values of $\frac{L}{\lambda}$ than the corresponding phase-locked states for a fixed $g_c = 400$ pS. However, note that for all possible dendritic lengths, the only single exchange in stability occurs at high somatic firing frequency and a large dendritic radius. Thus, the system displays qualitatively similar results when considering robustness to heterogeneity or robustness to noise, i.e., multiple exchanges in stability appear to be highly unlikely when considering changes in location of the electrical coupling.

8 Discussion

Many theoretical and experimental studies have provided evidence suggesting that electrical synapses aide in coordinating robust synchronous activity in networks of cortical inhibitory neurons. Most of the theoretical studies assume the electrical

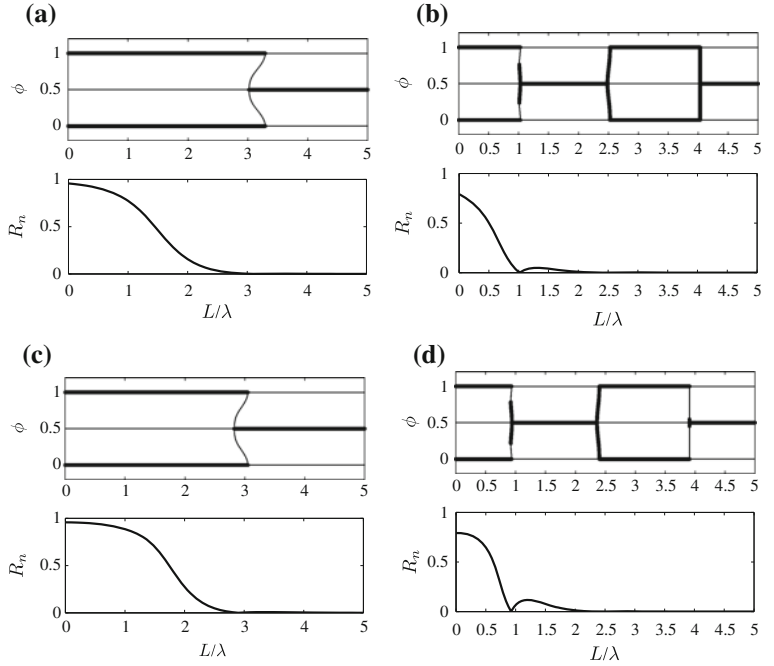

Fig. 12 Stability and robustness of phase-locking to noise for a fixed coupling conductance. Stability and robustness of the phase-locked states are plotted as a function of $\frac{L}{\lambda}$ when the conductance of the electrical coupling is 400 pS and the somata are firing at a frequency of 31 Hz (**a**, **c**) and 94 Hz (**b**, **d**). The radius of the dendrite is 0.2 μm in **a** and **b** and 2 μm in **c** and **d**. The *upper panels* plot the stability of the phase-locked solutions of Eq. (19). The stable phase-locked states are plotted as *thick lines* while the unstable states are plotted as *thin lines*. The *lower panels* plot the robustness of the phase-locked states where robustness is measured using the Kuramoto index R_n. Note that the effects of noise on phase-locked states and robustness are qualitatively similar to the effects of heterogeneity in intrinsic frequency (see Fig. 4)

synapses are located directly between the somata. The recent experimental findings that these inhibitory neurons are highly interconnected by electrical synapses located on their dendrites leads to the question of whether or not dendro-dendritic electrical synapses facilitate robust synchronous oscillatory behavior (Amitai et al. 2004; Fukuda and Kosaka 2000, 2003; Fukuda et al. 2006). Although a few modeling studies have examined the effects of dendritic properties on the existence and stability of phase-locking in dendritically coupled neurons (see Lewis and Skinner 2012), the robustness of these phase-locked states to heterogeneity and noise has not been explored in detail. In order to gain insight into the role that dendro-dendritic electrical coupling plays in generating synchronous oscillatory behaviour, we use the theory of weakly coupled oscillators to examine phase-locking in an electrically coupled pair of ball-and-stick model neurons. Our study focuses on how dendritic filtering and the location of the electrical synapse affect the existence, stability and robustness of phase-locked states.

Using published estimates of the electrical coupling conductance between two cortical inhibitory neurons $g_c = 400$ pS (Amitai et al. 2004; Beierleinet al. 2000; Gibson et al. 2005; Connors and Long 2004), our analysis reveals that the position of the

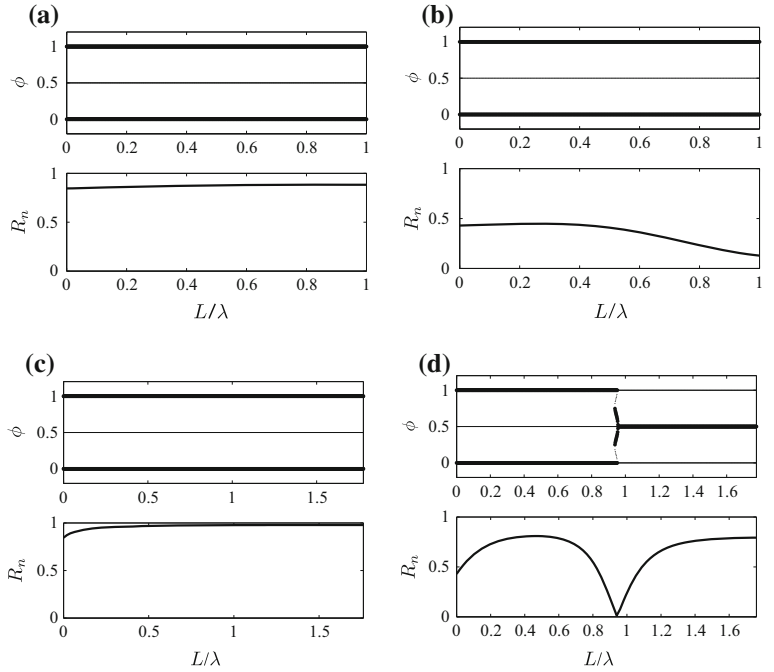

Fig. 13 Stability and robustness of phase-locking to noise for a fixed coupling coefficient. Stability and robustness of the phase-locked states are plotted as a function of $\frac{L}{\lambda}$ when the coupling coefficient is fixed at $CC = 0.05$ and the somata are firing at a frequency of 31 Hz (**a**, **c**) and 94 Hz (**b**, **d**). The radius of the dendrite is 0.2 μm in **a** and **b** and 2 μm in **c** and **d**. The *upper panels* plot the stability of the phase-locked solutions of Eq. (19). The stable phase-locked states are plotted as *thick lines* while the unstable states are plotted as *thin lines*. The *lower panels* plot the robustness of the phase-locked states where robustness is measured using the Kuramoto index R_n. Note that the effects of noise on phase-locked states and robustness are qualitatively similar to the effects of heterogeneity in intrinsic frequency (see Fig. 7)

electrical coupling plays an important role in determining the existence and stability of the synchronous and anti-phase states. As the location of the electrical synapse occurs further away from the somata, multiple exchanges in stability between the synchronous and anti-phase states can arise. However, the robustness of the phase-locked states in this case decreases rapidly towards zero as the distance between the electrical coupling and the somata increases. For all the parameters we examined, robustness to heterogeneities in intrinsic firing frequencies decays to ∼0.5 % by the time $\frac{L}{\lambda} = 2$. The rapidness of the decay in robustness suggests that multiple exchanges in stability are unlikely to be observed in real neurons. However, it is important to note that the published estimates of g_c (as cited above) are calculated from the experimentally measured coupling coefficient (CC) based on a single-compartment description of a neuron (Bennett 1977), which neglects spatial properties. As such, $g_c = 400$ pS may be a severe underestimate of the actual value of the electrical coupling conductance when it is located on the distal dendrites (Prinz and Fromherz 2002). With this in mind, we re-examine the stability and robustness of phase-locking using a fixed value of the experimentally measured coupling coefficient rather than a fixed g_c. Specifically,

we take $CC = 0.05$ (Amitai et al. 2004) and use ball-and-stick model neurons to derive the corresponding g_c (Prinz and Fromherz 2002). As expected, we find that the phase-locked states are less robust for more proximal coupling positions and more robust for more distal coupling positions for fixed $CC = 0.05$ as compared to the corresponding phase-locked states for a fixed $g_c = 400$ pS. Curiously, with a fixed $CC = 0.05$, no exhanges in stability with changing coupling position are observed except for a single exchange which was found in the extreme case of a high somatic firing frequency and a large dendritic radius. Furthermore, the existence of 1:1 phase-locking is fragile to asymmetries in dendritic length. We also show that the same results hold qualitatively when considering robustness of phase-locking to noise. Thus, our analysis for both fixed g_c and fixed CC suggest that multiple exchanges in stability between the synchronous and anti-phase states with changing coupling position are unlikely to be observed in real neural systems.

The present study builds off previous work that has examined the existence and stability of phase-locking in neurons with passive dendrites (Bressloff and Coombes 1997; Crook et al. 1998; Lewis and Rinzel 2004; Remme et al. 2009). These studies find that the position of coupling along the dendrite is an important factor in determining phase-locking behavior. In particular, Crook et al. (1998) and Bressloff and Coombes (1997) examine how the position of dendro-dendritic *chemical synapses* affect the phase-locking behavior in networks of neuronal oscillators. Similar to the present study, they find interesting exchanges in the stability of the synchronous and anti-phase phase-locked states with changing coupling position, and they provide explanations for this behavior in terms of filtering properties of the dendrite. A crucial difference between the current work and all of the previous studies listed above is our systematic examination of the robustness of the phase-locked states to heterogeneity and noise. Our results on neurons coupled by electrical synapses suggests that the robustness of the multiple exchanges in stability observed in neurons coupled by chemical synapses warrants further investigation.

We have modeled the dendrite of each neuron as a single passive cable. Thus, we have neglected the detailed branching structure of dendritic trees and the fact that the dendrites of some neurons possess high levels of active voltage-gated conductances (Johnston and Narayanan 2008). In terms of dendritic structure, we expect that the addition of realistic morphologies will not fundamentally change our basic results. Indeed one could calculate the filtering coefficients corresponding to a more complex passive dendritic tree (Bressloff and Coombes 1997), however, the filtering coefficients obtained will be very similar to those of a single branch (i.e., attenuation factors will decrease and the magnitudes of the phase-shifts will increase with increases in the electrotonic distance between the somata, $2\frac{L}{\lambda}$, and in the somatic firing frequency, ω). In fact, if dendritic trees follow Rall's $3/2$ rule, then each dendritic tree can be reduced to an equivalent cylinder (Rall 1959). Furthermore, similar to the results we present using the ball-and-stick model, studies using detailed multicompartment models of hippocampal inhibitory neurons have demonstrated that the location of dendro-dendritic electrical synapses plays an important role in determining network synchronization (Saraga et al. 2006; Saraga and Skinner 2004; Zahid and Skinner 2009). In particular, Saraga et al. (2006) find that synchronization of neurons with passive dendrites required extremely large coupling conductances when the electrical

synapses are located on the distal dendrites and that 1:1 phase-locking was very fragile to heterogeneities in this case. In terms of dendritic nonlinearities, Saraga et al. (2006) and others (Saraga and Skinner 2004; Traub et al. 2001; Zahid and Skinner 2009) also show that active dendritic conductances strongly facilitate robust synchronization of electrically coupled heterogeneous cells. As such, we expect the inclusion of active dendritic currents in our model to increase the robustness of the phase-locked states. In fact, active dendritic currents may also significantly change the synchronization properties. However, we note that recent experimental findings show that the dendrites of hippocampal fast-spiking inhibitory neurons express sodium channels at low density, if at all (Hu et al. 2010). Therefore, the dendrites in these neurons should be well modeled by passive or weakly nonlinear cables.

Acknowledgments This work was supported by the National Science Foundation under grant DMS-0921039. MS is supported by NIH grant T32-MH065214-1 through the Princeton Neuroscience Institute. The authors would also like to thank Jiawei Zhang for comments on the manuscript.

Appendix A: Somatic model and system parameters

We used a model of a cortical inhibitory fast spiking interneuron due to Erisir et al. (1999) to describe our somatic dynamics. The model equations and parameters are

$$\begin{aligned}
C_m \frac{dv}{dt} &= -g_{Na} m^3 h(v(t) - E_{Na}) - g_K n^2 (v(t) - E_K) - g_{K_s} n_s^4 (v(t) - E_K) \\
&\quad -g_L (v(t) - E_L) + I \\
\frac{dm}{dt} &= \alpha_m(v)(1 - m) - \beta_m(v) m \\
\frac{dh}{dt} &= \alpha_h(v)(1 - h) - \beta_h(v) h \\
\frac{dn}{dt} &= \alpha_n(v)(1 - n) - \beta_n(v) n \\
\frac{dn_s}{dt} &= \alpha_{n_s}(v)(1 - n_s) - \beta_{n_s}(v) n_s
\end{aligned}$$

where

$$\begin{aligned}
\alpha_m(v) &= \frac{40.0(75.5 - v)}{\exp((75.0 - v)/(13.5)) - 1.0} & \beta_m(v) &= \frac{1.2262}{\exp(v/42.248)} \\
\alpha_h(v) &= \frac{0.0035}{\exp(v/24.186)} & \beta_h(v) &= \frac{-0.017(51.25 + v)}{\exp(-(52.25 + v)/5.2) - 1.0} \\
\alpha_n(v) &= \frac{(95.0 - v)}{\exp((95.0 - v)/11.8) - 1.0} & \beta_n(v) &= \frac{0.025}{\exp(v/22.22)} \\
\alpha_{n_s}(v) &= \frac{-0.014(44.0 + v)}{\exp(-(44.0 + v)/2.3) - 1.0} & \beta_{n_s}(v) &= \frac{0.0043}{\exp((44.0 + v)/34.0)}
\end{aligned}$$

and

$$C_m = 1.0\mu\text{F/cm}^2 \quad g_{Na} = 112.5\ \text{mS/cm}^2 \quad g_K = 225mS/cm^2$$
$$g_{K_s} = 0.225\ \text{mS/cm}^2 \quad g_L = 0.25\ \text{mS/cm}^2 \quad E_{Na} = 74.0\ \text{mV}$$
$$E_K = -90.0\ \text{mV} \quad E_L = -70.0\text{mV}$$

The cable parameters we hold constant are

$$g_{LD} = 0.2\ \text{mS/cm}^2 \quad d = 0.002\ \text{cm} \quad R_i = 0.1\ \text{k}\Omega\,\text{cm}$$

Appendix B: Coupling coefficient

Here we derive the directional coupling coefficient for two electrically coupled ball-and-stick neurons with heterogeneity in dendritic length. The equations are given by

$$C_m \frac{\partial \bar{v}_j}{\partial t} = \frac{a}{2R_i} \frac{\partial^2 \bar{v}_j}{\partial x^2} - g_{LD}(\bar{v}_j - E_{LD})$$
$$C_m \frac{\partial \bar{v}_j}{\partial t}(0,t) = -g_L(\bar{v}_j(0,t) - E_L) + I + \frac{a^2}{d^2 R_i} \frac{\partial \bar{v}_j}{\partial x}(0,t)$$
$$\frac{\pi a^2}{R_i} \frac{\partial \bar{v}_j}{\partial x}(L_j,t) = g_c(\bar{v}_k(L_k,t) - \bar{v}_j(L_j,t)).$$

If a current I is applied to the soma of cell j, the steady-state equations are then

$$\frac{d^2 v_j}{dx^2} = \frac{2R_i g_{LD}}{a}(v_j - E_{LD}) = \frac{1}{\lambda^2}(v_j - E_{LD})$$
$$\frac{a^2}{d^2 R_i} \frac{dv_j}{dx}(0) = g_L(v_j(0) - E_L) - I$$
$$\frac{dv_j}{dx}(L_j) = \frac{g_c R_i}{\pi a^2}(v_k(L_k) - v_j(L_j)),$$

where $v_j(x) = \bar{v}_j(x, \infty)$, $j,k = 1,2$; $j \neq k$. The solutions of the above system are given by

$$v_j(x) = A_j \sinh\left(\frac{x}{\lambda}\right) + B_j \cosh\left(\frac{x}{\lambda}\right) + E_{LD}$$
$$v_k(x) = A_k \sinh\left(\frac{x}{\lambda}\right) + B_k \cosh\left(\frac{x}{\lambda}\right) + E_{LD},$$

where

$$B_j = \frac{g_{LD}}{g_L} \varepsilon A_j + F + \frac{I}{g_L}$$

$$
\begin{aligned}
B_k &= \frac{g_{LD}}{g_L}\varepsilon A_k + F \\
A_j &= \frac{g}{\lambda}\frac{\gamma_k}{\alpha_j\alpha_k - \left(\frac{g}{\lambda}\right)^2\gamma_k\gamma_j}\left(\frac{g}{\lambda}\left[F + \frac{I}{g_L}\right]\cosh\left(\frac{L_j}{\lambda}\right) - F\beta_k\right) \\
&\quad + \frac{\alpha_k}{\alpha_j\alpha_k - \left(\frac{g}{\lambda}\right)^2\gamma_k\gamma_j}\left(\frac{g}{\lambda}F\cosh\left(\frac{L_k}{\lambda}\right) - \left[F + \frac{I}{g_L}\right]\beta_j\right) \\
A_k &= \frac{g}{\lambda}\frac{\gamma_j}{\alpha_j\alpha_k - \left(\frac{g}{\lambda}\right)^2\gamma_k\gamma_j}\left(\frac{g}{\lambda}F\cosh\left(\frac{L_k}{\lambda}\right) - \left[F + \frac{I}{g_L}\right]\beta_j\right) \\
&\quad + \frac{\alpha_j}{\alpha_j\alpha_k - \left(\frac{g}{\lambda}\right)^2\gamma_k\gamma_j}\left(\frac{g}{\lambda}\left[F + \frac{I}{g_L}\right]\cosh\left(\frac{L_j}{\lambda}\right) - F\beta_k\right),
\end{aligned}
$$

and

$$
\begin{aligned}
\alpha_j &= \left[\frac{1}{\lambda} + \frac{g_{LD}}{g_L}\frac{\varepsilon g}{\lambda}\right]\cosh\left(\frac{L_j}{\lambda}\right) + \left[\frac{g}{\lambda} + \frac{g_{LD}}{g_L}\frac{\varepsilon}{\lambda}\right]\sinh\left(\frac{L_j}{\lambda}\right) \\
\beta_j &= \frac{1}{\lambda}\sinh\left(\frac{L_j}{\lambda}\right) + \frac{g}{\lambda}\cosh\left(\frac{L_j}{\lambda}\right) \\
\gamma_j &= \sinh\left(\frac{L_j}{\lambda}\right) + \frac{g_{LD}}{g_L}\varepsilon\cosh\left(\frac{L_j}{\lambda}\right) \\
F &= E_L - E_{LD} \\
g &= \frac{g_c R_i \lambda}{\pi a^2} \\
\varepsilon &= \frac{a^2}{d^2 R_i g_{LD}\lambda},
\end{aligned}
$$

and α_k, β_k, and γ_k are defined similarly. The coupling coefficient is then $\frac{\Delta v_k(0)}{\Delta v_j(0)}$, i.e., the difference in the steady state potentials for the two somata when current I is injected into the soma of cell j and no current is injected into either cell. Let the coefficients $\tilde{A}_j$, $\tilde{A}_k$, $\tilde{B}_j$ and $\tilde{B}_k$ correspond to the steady state potentials when no current is injected into either cell (i.e., set $I = 0$ in the equations for A_j, A_k, B_j and B_k). Then the directional coupling coefficient that measures the DC attenuation from cell j to cell k is

$$
\begin{aligned}
CC_k &= \frac{\Delta v_k(0)}{\Delta v_j(0)} = \frac{B_k - \tilde{B}_k}{B_j - \tilde{B}_j} \\
&= \frac{\frac{g_{LD}}{g_L}\varepsilon\frac{g}{\lambda}\rho\left(-\gamma_j\beta_j + \alpha_j\cosh\left(\frac{L_j}{\lambda}\right)\right)}{\frac{g_{LD}}{g_L}\varepsilon\rho\left(\left(\frac{g}{\lambda}\right)^2\gamma_k\cosh\left(\frac{L_j}{\lambda}\right) - \alpha_k\beta_j\right) + 1},
\end{aligned}
$$

where

$$\rho = \frac{1}{\alpha_k \alpha_j - \left(\frac{g}{\lambda}\right)^2 \gamma_k \gamma_j}.$$

If $L_j = L_k = L$, then we arrive at the coupling coefficent for two identical ball-and-stick neurons

$$CC = \frac{2\varepsilon g_{LD} g}{g_L + \sinh\left(2\frac{L}{\lambda}\right)\left[\varepsilon g_{LD} + 2g g_L\right] + \cosh\left(2\frac{L}{\lambda}\right)\left[2\varepsilon g g_{LD} + g_L\right]}.$$

Furthermore, if $\frac{L}{\lambda} = 0$, we arrive at

$$\begin{aligned} CC &= \frac{\varepsilon g_{LD} g}{g_L + \varepsilon g_{LD} g} \\ &= \frac{g_c}{\pi d^2 g_L + g_c}, \end{aligned}$$

which is the coupling coefficient assuming two coupled single-compartment neurons Bennett (1977).

References

Amitai Y, Gibson JR, Beierlein M, Patrick PL, Ho AM, Connors BW, Golomb D (2004) The spatial dimensions of electrically coupled networks of interneurons in the neocortex. J Neurosci 22(10): 4142–4152

Averbeck BB, Lee D (2004) Coding and transmission of information by neural ensembles. Trends Neurosci 27(4):225–230

Beierlein M, Gibson JR, Connors BW (2000) A network of electronically coupled interneurons drives synchronized activity in neocortex. Nat Neurosci 3:904–910

Bennett MVL (1977) The nervous system, part I. In: Brookhart JM, Mountcastle VB (eds) Handbook of physiology, section I. American Physiological Society, Bethesda, pp 357–416

Bressloff PC, Coombes S (1997) Physics of the extended neuron. J Mod Phys B 11:2343–2392

Bressloff PC, Coombes S (1997) Synchrony in an array of integrate-and-fire neurons with dendritic structure. Phys Rev Lett 78:4665–4668

Buzsáki G (1997) Functions for hippocampal interneurons. Can J Physiol Pharm 75:508–515

Buzsáki G, Draguhn A (2004) Neuronal oscillations in cortical networks. Science 304(5679):1926–1929

Cardin JA, Carleń M, Meletis K, Knoblich U, Zhang F, Deisseroth K, Tsai L, Moore CI (2009) Driving fast-spiking cells induces gamma rhythm and controls sensory responses. Nature 459:663–667

Connors BW, Long MA (2004) Electrical synapses in the mammalian brain. Annu Rev Neurosci 27:393–418

Crook SM, Ermentrout GB, Bower JM (1998) Dendritic and synaptic effects in systems of coupled cortical oscillators. J Comput Neurosci 5:315–329

Erisir A, Lau D, Rudy B, Leonard CS (1999) Function of specific K+ channels in sustained high-frequency firing of fast-spiking neocortical interneurons. J Neurophysiol 82:2476–2489

Ermentrout B, Pascal M, Gutkin B (2001) The effects of spike frequency adaptation and negative feedback on the synchronization of neural oscillators. Neural Comput 13(6):1285–1310

Ermentrout GB (1996) Type 1 membranes, phase resetting curves, and synchrony. Neural Comput 8: 979–1001

Ermentrout GB, Kopell N (1984) Frequency plateaus in a chain of weakly coupled oscillators, I. SIAM J Math Anal 15(2):215–237

Fink C, Booth V, Zochowski M (2011) Cellularly-driven differences in network synchronization capacity are differentially modulated by firing frequency. PLOS Comput Biol 7(5):e1002062

Fukuda T, Kosaka T (2000) Gap junctions linking the dendritic network of gabaergic interneurons in the hippocampus. J Neurosci 20:1519–1528
Fukuda T, Kosaka T (2003) Ultrastructural study of gap junctions between dendrites of parvalbumin-containing gabaergic neurons in various neocortical areas of the adult rat. Neuroscience 120:5–20
Fukuda T, Kosaka T, Singer W, Galuske RAW (2006) Gap junctions among dendrites of cortical gabaergic neurons establish a dense and widespread intercolumnar network. J Neurosci 26:3434–3443
Galaretta M, Hestrin S (1999) A network of fast spiking cells in the neocortex connected by electrical synapses. Nature 402:72–75
Gibson JR, Beierlein M, Connors BW (1999) Two networks of electrically coupled inhibitory neurons in neocortex. Nature 402:75–79
Gibson JR, Beierlein M, Connors BW (2005) Functional properties of electrical synapses between inhibitory interneurons of neocortical layer 4. J Neurosci 93:467–480
Gonzalez-Burgos G, Lewis DA (2008) Gaba neurons and the mechanisms of network oscillations: Implications for understanding cortical dysfunction in schizophrenia. Schizophrenia Bull 34(5):944–961
Hestrin S, Galarreta M (2005) Electrical synapses define networks of neocortical gabaergic neurons. Trends Neurosci 28:304–309
Hoppensteadt FC, Izikevich EM (1997) Weakly connected neural networks. Springer, New York
Hu H, Martina M, Jonas P (2010) Dendritic mechanisms underlying rapid synaptic activation of fast-spiking hippocampal interneurons. Science 327:52–58
Johnston D, Narayanan R (2008) Active dendrites: colorful wings of the mysterious butterfly. Trends Neurosci 31(6):309–316
Koch C (1999) Biophysics of computation: information processing in single neurons. Oxford University Press, New York
Kopell N, Ermentrout GB (2003) Chemical and electrical synapses perform complementary roles in the synchronization of interneuronal networks. Proc Natl Acad Sci 101:15482–15487
Kuramoto Y (1984) Chemical oscillations, waves, and turbulence. Springer, Berlin
Lewis TJ, Rinzel J (2003) Dynamics of spiking neurons connected by both inhibitory and electrical coupling. J Comput Neurosci 14:283–309
Lewis TJ, Rinzel J (2004) Dendritic effects in networks of electrically coupled fast-spiking interneurons. Neurocomputing 58–60:145–150
Lewis TJ, Skinner FK (2012) Understanding activity in electrically coupled networks using PRCs and the theory of weakly coupled oscillators. In: Schultheiss NW, Prinz A, Butera RJ (eds) Phase response curves in neuroscience: theory, experiment, and analysis. Springer, New York, pp 329–359
Mainen ZF, Sejnowski TJ (1996) Influence of dendritic structure on firing pattern in model neocortical neurons. Nature 382:363–366
Mancilla JG, Lewis TJ, Pinto DJ, Rinzel J, Connors BW (2007) Synchronization of electrically coupled pairs of inhibitory interneurons in neocortex. J Neurosci 27(8):2058–2073
Mann EO, Paulsen O (2005) Mechanisms underlying gamma (40 Hz) network oscillations in the hippocampusa mini-review. Prog Biophys Mol Biol 87(1):67–76
McBain CJ, Fisahn A (2001) Interneurons unbound. Nat Rev 2:11–23
Netoff T, Schwemmer MA, Lewis TJ (2012) Experimentally estimating phase response curves of neurons: theoretical and practical issues. In: Schultheiss NW, Prinz A, Butera RJ (eds) Phase response curves in neuroscience: theory, experiment, and analysis. Springer, New York, pp 95–129
Neu JC (1979) Coupled chemical oscillators. SIAM J Appl Math 37(2):307–315
Ono T, Sasaki K, Nishino H, Fukuda M, Shibata R (1986) Feeding and diurnal related activity of lateral hypothalamic neurons in freely behaving rats. Brain Res 373(1–2):92–102
Pfeuty B, Mato G, Golomb D, Hansel D (2003) Electrical synapses and synchrony: the role of intrinsic currents. J Neurosci 23(15):6280–6294
Pfeuty B, Mato G, Golomb D, Hansel D (2005) The combined effects of inhibitory and electrical synapses in synchrony. Neural Comput 17:633–670
Prinz AA, Fromherz P (2002) Effect of neuritic cables on conductance estimates for remote electrical synapses. J Neurophysiol 89:2215–2224
Rall W (1957) Membrane time constants of motoneurons. Science 126:454
Rall W (1959) Branching dendritic trees and motoneuron membrane resistivity. Exp Neurol 2:491–527
Rall W (1960) Membrane potential transients and membrane time constant of motoneurons. Exp Neurol 2:503–532

Rall W (1977) Time constants and electrotonic length of membrane cylinders and neurons. In: Brookhart JM, Mountcastle VB (eds) Handbook of physiology. The nervous system I. American Physiological Society, Bethesda

Rekling JC, Feldman JL (1998) Pre-bötzinger complex and pacemaker neurons: hypothesized site and kernel for respiratory rhythm generation. Annu Rev Physiol 60:385–405

Remme M, Lengyel M, Gutkin BS (2009) The role of ongoing dendritic oscillations in single-neuron dynamics. PLoS Comput Biol 5(9):e1000493

Risken H (1989) The Fokker–Planck equation: methods of solution and applications. Springer, New York

Salinas E, Sejnowski TJ (2001) Correlated neuronal activity and the flow of neural information. Nat Rev Neurosci 2:539–550

Saraga F, Ng L, Skinner FK (2006) Distal gap junctions and active dendrites can tune network dynamics. J Neurophysiol 95:1669–1682

Saraga F, Skinner FK (2004) Location, location, location (and density) of gap junctions in multi-compartment models. Neurocomputing 58–60:713–719

Schwemmer MA, Lewis TJ (2011) Effects of dendritic load on the firing frequency of oscillating neurons. Phys Rev E 83:013906

Schwemmer MA, Lewis TJ (2012) Bistability in a leaky-integrate-and-fire neuron with a passive dendrite. SIAM J Appl Dyn Syst 11:507–539

Schwemmer MA, Lewis TJ (2012) The theory of weakly coupled oscillators. In: Schultheiss NW, Prinz A, Butera RJ (eds) Phase response curves in neuroscience: theory, experiment, and analysis. Springer, New York, pp 3–32

Sohal VS, Zhang F, Yizhar O, Deisseroth K (2009) Parvalbumin neurons and gamma rhythms enhance cortical circuit performance. Nature 459:698–702

Stratonovich RL (1967) Topics in the theory of random noise. Gordon and Breach, New York

Teramae J, Nakao H, Ermentrout GB (2009) Stochastic phase reduction for a general class of noisy limit cycle oscillators. Phys Rev Lett 102:194102

Teramae J, Tanaka D (2004) Robustness of the noise-induced phase synchronization in a general class of limit cycle oscillators. Phys Rev Lett 93(20):204103

Traub RD, Kopell N, Bibbig A, Buhl E, LeBeau FEN, Whittington MA (2001) Gap junctions between interneuron dendrites can enhance synchrony of gamma oscillations in distributed networks. J Neurosci 21(23):9478–9486

Tresch MC, Kiehn O (2002) Synchronization of motor neurons during locomotion in the neonatal rat: predictors and mechanisms. J Neurosci 22(22):9997–10008

van Kampen NG (1981) Stochastic processes in physics and chemistry. Elsevier Science, Amsterdam

Wang X-J, Buzsáki G (1996) Gamma oscillation by synaptic inhibition in a hippocampal interneuronal network model. J Neurosci 16(20):6402–6413

Ward LM (2003) Synchronous neural oscillations and cognitive processes. Trends Cogn Sci 7(12):553–559

Zahid T, Skinner FK (2009) Predicting synchronous and asynchronous network groupings of hippocampal interneurons coupled with dendritic gap junctions. Brain Res 1262:115–129